



GENERAL ASPECTS OF CALIBRATION OF THE
MÜNSTER DUAL PHASE XENON TPC

GENERELLE ASPEKTE DER KALIBRATION DER
MÜNSTER XENON ZWEIPHASEN-TPC

BACHELORTHESES

Nicolai Krybus

Westfälische Wilhelms-Universität Münster

Institut für Kernphysik

AG Weinheimer

Themensteller: Prof. Dr. C. Weinheimer

Zweitgutachter: Prof. Dr. A. Kappes

Münster, Oktober 2016

Eidesstattliche Erklärung

Hiermit versichere ich, *Nicolai Krybus*, dass ich die vorliegende Arbeit selbstständig verfasst und keine anderen als die angegebenen Quellen und Hilfsmittel verwendet habe. Gedanklich, inhaltlich oder wörtlich übernommenes habe ich durch Angabe von Herkunft und Text oder Anmerkung belegt bzw. kenntlich gemacht. Dies gilt in gleicher Weise für Bilder, Tabellen, Zeichnungen und Skizzen, die nicht von mir selbst erstellt wurden.

Münster, 21. Oktober 2016

Nicolai Krybus

Contents

1	Introduction	1
2	The Muenster dual phase xenon TPC	3
2.1	The Hamamatsu R8520-06-AL PMTs	5
2.2	Scintillation and ionisation of xenon	5
2.3	Energy calibration sources	6
2.4	Data acquisition (DAQ) at the Muenster xenon TPC	8
3	PMT gain calibration	11
3.1	Operating principle of a PMT	11
3.2	Introduction to LED gain calibration	13
3.3	LED gain calibration	16
3.3.1	Single photoelectron peak fit	16
3.3.2	Double and triple photoelectron peak fit	19
3.3.3	Results of the LED gain calibration	21
3.3.4	Comparing the measured events to the expectations from Poisson statistic	23
4	Energy calibration	27
4.1	Preparation and measuring	27
4.2	Analysis of the ^{137}Cs measurement	27
5	Conclusion and outlook	35
A	Appendix	37
A.1	Histograms of the PMTs	38
A.2	Parameters used for the fits	51
A.3	Example of a S1-S2 event	52
	Bibliography	53

1 Introduction

Today physicists agree on the point that our universe consists not only of visible matter. Visible, baryonic matter makes only 4.9% of the total energy of our universe. The rest consists of around 26.8% dark matter and 68.3% dark energy [1]. As of now, dark energy is still a big mystery, with almost no information. However, physicists developed many theories about the nature of dark matter, some of which could even be verifiable with the available techniques.

One of the most promising theories about dark matter revolves around a *Weakly Interactive Massive Particle* (WIMP), a hypothetical particle that is subject of current research and scientific discussion that would apply as so called “cold” dark matter. The theory of a WIMP is special in the way that it is theoretically possible to be detected with already existing technology. However as its name says, interactions between WIMPs and baryonic mass are rare. WIMPs are expected to have energies in the order of magnitudes around GeV, and therefore travel with velocities below the speed of light. Similar to neutrinos, WIMPs might surpass the earth or other large structures of baryonic matter without a single interaction.

The now fully functional XENON1T experiment makes a further step towards finding dark matter and then exploring its characteristics. It is the latest expansion of the XENON Dark Matter Project, an international research group, resident at the Laboratori Nazionali del Gran Sasso (LNGS) and it is one of the leading experiments in terms of sensitivity for WIMPs. The XENON experiments use dual phase time projection chambers (TPC) filled with liquid xenon (LXe) and a gaseous phase of xenon on top to detect WIMPs scattering off the nuclei of the detector material through emitted light and charge. After XENON10 with 25 kg of Xe and XENON100 with 161 kg the detector has now reached a detection volume of 3500 kg of LXe which severely increases the sensitivity. XENON100, which started 2008, reached a sensitivity limit of $2 \times 10^{45} \text{ cm}^2$ for WIMP mass of $55 \text{ GeV}/c^2$ [2] in 62 kg of fiducial volume. XENON1T further increases the limit by two orders of magnitude up to $1.6 \times 10^{-47} \text{ cm}^2$ for $50 \text{ GeV}/c^2$ [3] in 1 t fiducial volume.

In 2011 the group of Prof. Dr. C. Weinheimer at the University of Muenster built its own

TPC on a much smaller scale to further investigate this detector setup [4]. The *Muenster xenon dual phase TPC* contains a target mass of 2.56 kg and can be operated in a similar way as its bigger incarnation at LNGS. Although it will never be able to prove detecting a WIMP due to its small detection volume, it can be used to learn about detector calibration or xenon purification. At first, the 14 implemented PMTs have to be tested on their response to incident photons. For energy calibration purposes, radioactive sources, which are placed in range of the detector, are used. As the radiation of the radioactive sources is almost perfectly known, those can be used to scale the outputs of the detector.

This bachelor thesis revolves around the calibration of the detector setup. At first, the setup of the *Muenster xenon dual phase TPC* will be introduced. After the general setup is explained, the photomultipliers (PMT) used inside the detector and the method used to calibrate the PMTs via a low intensity LED pulser will be explained. After finishing the calibration of the PMTs by determining each PMTs response to a single incident photon, the energy calibration of the detector can be done, using ^{137}Cs as a radioactive gamma calibration source. The energy calibration is used to determine the light yield of the detector, implying the amount of detected photons at the PMTs compared to the energy of the incident particle. The analysis of the light yield was not unequivocal but shows that the detector is able to detect approximately one photon per keV energy.

2 The Muenster dual phase xenon TPC

Time projection chambers (TPC) are used to not only detect a certain particle, but additionally determine the position of the interaction inside the detector. Typical TPCs have a cylindrical detection volume, filled with gas, liquid or a combination of both. The detection volume is placed inside an electric field, which drifts electrons, produced by ionization, into a certain direction.

The *Muenster xenon TPC* is constructed as a cylindrical volume filled with xenon, as can be seen in figure 2.1. The volume has a height of 170 mm and a diameter of 80 mm and is made of polytetrafluoroethylene (PTFE), also known as Teflon[®], due to its high reflectivity for 178 nm photons and low radioactivity. The inner TPC is surrounded by a larger cylinder made of stainless steel, which holds the TPC in an insulating vacuum. A cooling system attached to the TPC makes it possible to precisely regulate the temperature of the target volume and by this also regulate the pressure inside the detector and the phase of the xenon. Usually the *Muenster xenon TPC* would run at around -98 °C and two bar pressure, resulting in a liquid phase of xenon at the bottom of the TPC and a gaseous phase above. On the top and at the bottom of the detector there are seven photomultiplier tubes (PMTs) each to detect scintillation and ionization signals from the target mass. The PMTs are able to detect light signals at the xenon wavelength of 178 nm. The working principle of a PMT will be explained in more detail in a further section. To enable an electric drift field, a cathode and anode pair is implemented inside the TPC with the cathode at the bottom. The liquid level is supposed to be just below the anode during measurements. In order to protect the PMTs from flash-overs from the anode and cathode at the bottom and the top, meshes are installed right before them. Outside of the cylinder there are twelve copper rings to shape the electric field inside the TPC to be homogeneous on every point.

If a particle enters the TPC at liquid level, it interacts with the xenon atoms, which then emit scintillation and ionization signals. The light signal, called S1-signal, is instantly detected by all PMTs as it travels with the speed of light. As it gets partly reflected at the liquid surface of the xenon, the bottom PMTs will detect a larger signal. The emitted electrons get drifted

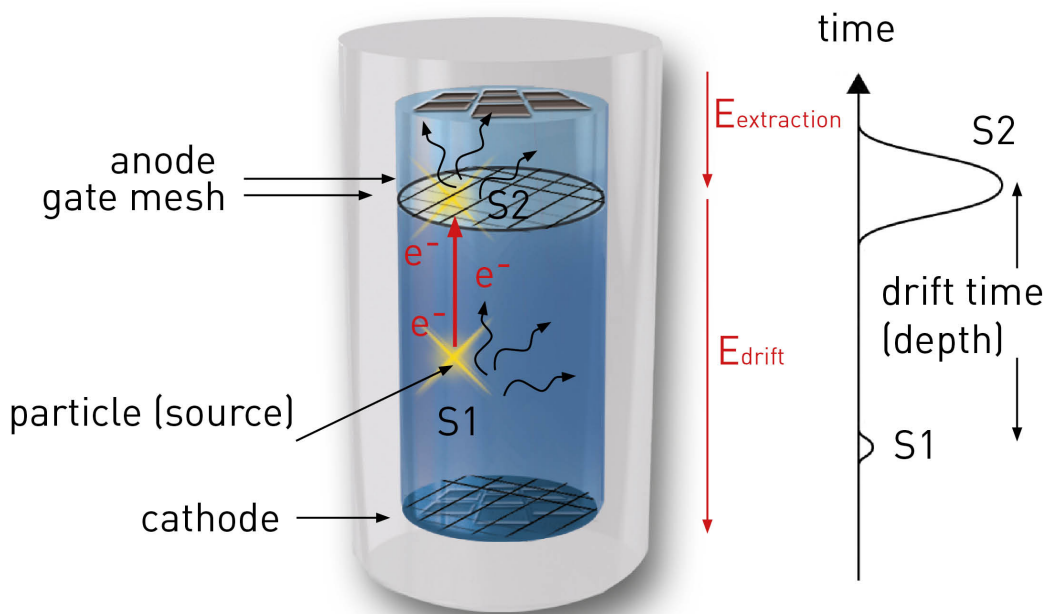


Figure 2.1: Sketch of the Münster TPC setup to illustrate the working principle. The detection volume is represented by the two blue cylinders, with the liquid phase in darker color at the bottom below the anode and the gate mesh. Incoming particles cause scintillation light (S1) and electrons from ionization that further produce additional scintillation light (S2). The signals get detected by the 14 PMTs, each seven at the top and the bottom of the TPC, in a 2-3-2 array. The sketch is not to scale in every detail.

by the electric field E_{drift} towards the gas phase and the top PMTs. E_{drift} runs with an electric field strength of about 0.7 kV/cm. As soon as they reach the gas phase, they get extracted by the second electric field $E_{extraction}$ and start producing scintillation light, which is detected by the PMTs with a short delay to the S1. $E_{extraction}$ runs on a higher electric field strength with 8.8 kV/cm. The S2-signal gets seen mostly by the top PMTs with a very high intensity compared to the S1-signal. The positional reconstruction can be realized using the arrangement of the PMTs and the delay between S1 and S2. The z-coordinate (depth) can be calculated using the drift-time, due to the S1 traveling with the speed of light, whereas the S2 gets transmitted by electrons, where the velocity is dependent on the strength of the electric fields inside the TPC. At the current settings, the emitted electrons travel with about 2 mm/ μ s [5]. The x-/y-coordinates can be reconstructed by comparing the strength of the detected signal in each single PMT. Due to the electric fields the electrons will approximately only travel in vertical direction through the TPC and so the PMT right above the S2-signal will detect the strongest signal.

2.1 The Hamamatsu R8520-06-AL PMTs

The *Muenster xenon TPC* uses a PMT from *Hamamatsu*, the *R8520-06-AL*, which is specially developed for LXe detectors. The one inch square detector provides an effective area of 20.5 mm², covered by a synthetic silica window, which is transparent to the UV scintillation light of xenon. The photocathode is optimized for xenon scintillation light at a wavelength of 178 nm, providing a quantum efficiency of around 30% and has a spectral response from 160 nm to 650 nm. Incoming signals are amplified by ten dynode stages that are connected to a resistor chain. The PMTs are also designed to work properly in the cryogenic environment of the TPC. The operating temperature range of the PMTs goes from -100°C to 50°C and they are resistant to pressure up to 5 bar.

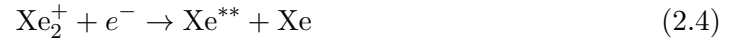
2.2 Scintillation and ionisation of xenon

Xenon has many advantages for the dark matter search over other common detector materials as silicon or argon. The first one is the heavy nucleus of xenon ($A=131$) [6], which gives xenon in comparison a higher spin-independent cross section at lower recoil energies. Further, xenon has a very high density at liquid state, around 3 g/cm³, which leads to xenon self-shielding itself from radiation while also reducing the size of the detector.

The biggest advantage is the transparency of xenon for its own scintillation photons. As the scintillation photons are emitted by an excited dimer state, the photons will not get absorbed by other xenon atoms. A scintillation photon gets emitted as the excited xenon dimer state decays to its ground state. There are two different ways to create the excited dimer state: The first way starts with a xenon atom getting excited by the incoming particle:



The second way follows an initial ionization of a xenon atom by the incoming particle which leads to the same outcome over the course of a few other reactions:



with equations referring to [5]. As the excited dimer state is only possible to find after an initial incoming particle reacted with a ground state xenon atom, the scintillation light will not get absorbed by other xenon atoms but travel uninterrupted through the detector. To produce one single scintillation photon in liquid xenon, an energy of $W = (21.61 \pm 0.21)$ eV [7] is required.

2.3 Energy calibration sources

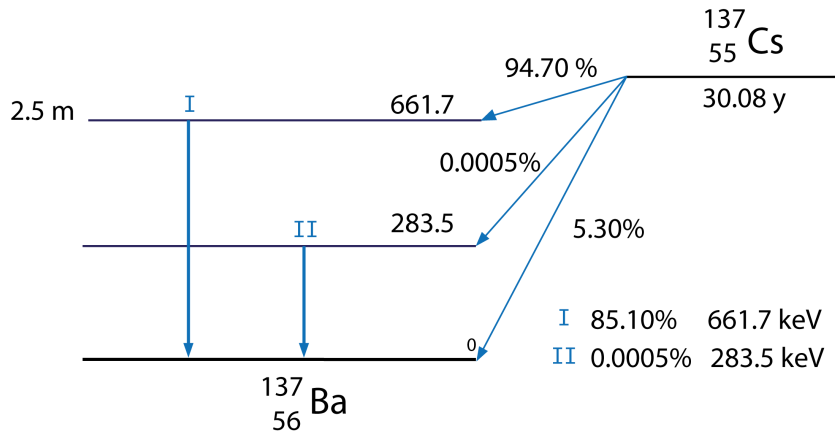


Figure 2.2: Sketch of the beta decay scheme of ^{137}Cs (with data from [8])

In order to enable an energy calibration of the *Muenster xenon TPC*, a mono-energetic source of photons is needed. In this case, this gets realized by a radioactive source placed outside of the detector. As already mentioned, liquid xenon has a very high density at around 3 g/cm^3 and a heavy nucleus at an atomic number of 54, which results in a very good self-shielding for gamma radiation. Additionally, the source has to penetrate the detectors shell as well as the vacuum chamber surrounding the detector and the cryostat vessel, which already eliminates the possibility of using alpha or beta sources as they would not be able to pass the vacuum chamber. Therefore, a high energetic gamma source, which is able to provide a sufficient

number of gammas up to the center of the detection volume, is needed. For this calibration ^{137}Cs is chosen as investigated with a dedicated GEANT4 simulation in [9]. ^{137}Cs has a β^- -decay to ^{137m}Ba that decays to ^{137}Ba by emitting a gamma with an energy of 662 keV with a half-life of 30.08 y [8]. Figure 2.2 shows the decay chain. Gammas that enter the

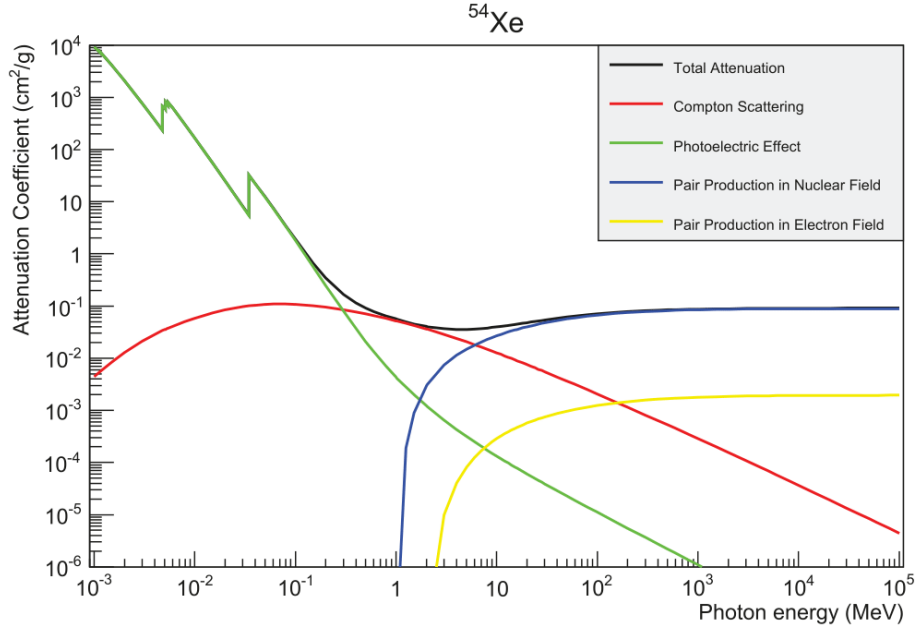


Figure 2.3: Attenuation Coefficient of photons in xenon plotted against the energy of the photon for photoelectric effect, Compton scattering and pair production [6].

detection volume have different possibilities of interacting with the detection material as is shown in figure 2.3. As can be seen, for photons of high energies the dominant interaction between the incident photons and xenon atoms is **pair production**. If the photon is in close vicinity of a xenon nucleus, the photon converts into an electron-positron pair, which keeps the momentum of the photon. The nucleus will also receive a recoil. In this case pair production does not have to be taken into account as ^{137}Cs decays only at 662 keV.

The second possible interaction is the **photoelectric effect**. It is especially dominant at low photon energies. In this case the photon collides with a xenon atom and in doing so gets completely absorbed. The energy of the photon gets used to liberate an electron from the atomic shell ionizing the atom in the process. In fact, the energy of the incident photon is more than just the binding energy of the electron, as a part of it goes into the recoil between nucleus and electron but will eventually be deposited inside the detector through further interactions with the xenon atoms.

The third interaction is **Compton scattering**. This means, that the incident photon recoils off the electrons in the shell of the xenon atoms. If a photon recoils on an electron it transfers a momentum and scatters with lower energy. The energy after the Compton scattering is dependent on the angular of the initial collision (see figure 2.4). Moreover

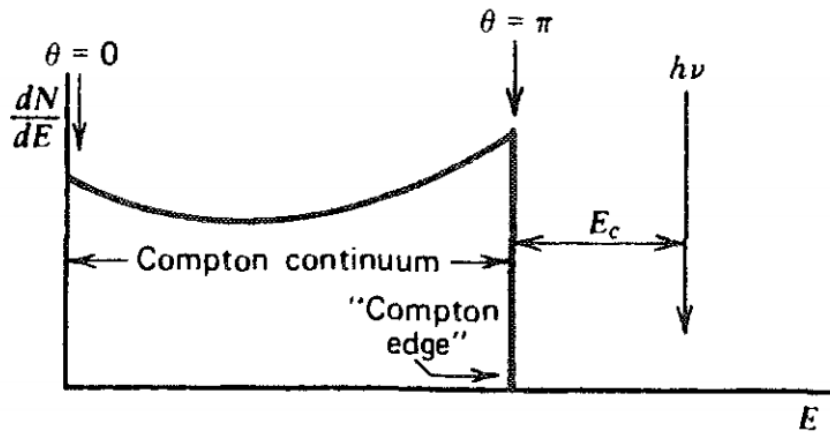


Figure 2.4: General shape of the electron energy distribution for Compton scattering interactions. It shows a continuous spectrum for electrons that scatter under the angle Θ , the Compton edge after 180° and the peak where the gamma gives its full energy to the electron. [10].

Compton scattering opens the possibility for multiple interactions with only a single photon as the scattered photon still can have enough energy to scatter again on a different atom. The end of this reaction would be marked by a photoelectric effect and by this the full absorption of the photon. Consequently the photon would place its full energy (in this case 662 keV) inside the detector. At any time during this chain of recoils the photon might scatter in a direction where it leaves the detection volume without depositing its full energy.

2.4 Data acquisition (DAQ) at the Muenster xenon TPC

In a first step, signals detected by the PMTs inside the *Muenster xenon TPC* are sent to a 16 channel CAEN Mod. N979 fast-amplifier, where the signals get amplified by a factor of 10. Further, the *Muenster xenon TPC* uses two CAEN V1724-boards to record the waveforms of the signal of each PMT. The boards have 14 bits, so the signal can reach up to $2^{14} = 16384$ ADC units (analog to digital converter units) per sample. The boards further have 2.25 V input range, 100 MHz and 8 channels each for input. As later described in chapter 3.1 the PMTs recognize signals of photons as a drop in potential, so the baseline for the input channels has to be set high enough as the peak goes in negative direction. The boards are controlled using the software FPPDAQ by Volker Hannen, which also saves the ADC values for each waveform in raw data event files (.eve files) and also sets the baseline to a sufficient level. The ADC values can be converted to voltage values using

$$U_V = U_{ADC} \cdot \frac{U_{ir}}{2^n}, \quad (2.8)$$

with the desired signal voltage U_V , the signal voltage in ADC units U_{ADC} , the input range of the *CAEN* boards U_{ir} and the number of bits n . In this case the conversion factor from ADC units to Volt is 0.137 mV.

Depending on the intended measurement the DAQ can be operated with an external or an internal trigger mode. Usually the TPC would use the *CAENs* internal trigger threshold for measurement when the trigger signal is given to both boards simultaneously. In case of the measurements for ^{137}Cs a window of 16,000 samples would be saved, 8,000 of which are right after the trigger signal and the remaining 8,000 before, after every signal that exceeds a intensity of 6,000 ADC units.

To control the UV LED pulser for the gain calibration later on, the *Muenster xenon TPC* uses an external trigger, which is generated by the *AFG3102* pulse generator of *Tektronix*. The trigger is connected to the boards and the LED simultaneously. For each acquisition window the trigger is set to the 256th sample in the middle of the window (512 samples in total). The first 50 events of the window are taken with background only to enable a baseline subtraction (see chapter 3.2). In order to create the histograms for the gain calibration, the data needs to be processed as described in section 3.2. The necessary steps are performed by the *C++* script *wfview* which transforms the event files into simple text files with 14 columns, one for each PMT, and a row for each event with the measured charges in it.

Otherwise, to process data from the *Muenster xenon TPC* the program *Processor for analyzing XENON data (PAX)* is used [12]. It was developed by the XENON collaboration to analyze data from TPCs of variable dimension. *PAX* is used to identify S1 and S2 signals by using multiple steps: the first step is classifying the data taken during a trigger into events. Inside the events *PAX* searches for pulses and classifies them as hits if they exceed a previously chosen baseline. Further, hits get clustered to a peak, if *PAX* identifies them as having the same origin. If both a S1- and a corresponding S2 peak are found they are matched as an interaction.

Another important value, especially for the energy calibration, is the light yield (LY) [2] of the detector, which is the number of collected photons by the PMTs for one keV recoil energy. The LY is used to transform PMT output into energy values.

All data used in this thesis were collected in cooperation with Michael Murra and might reappear in his future works.

3 PMT gain calibration

In order to evaluate the results of a measurement, the calibration of the PMTs is of utmost importance. One can observe that each PMT has a characteristic response to incident photons and in order to link the output to the input a calibration is required. To calibrate the PMTs, the amount of photoelectrons induced by a single photon, the gain, needs to be investigated. The gain can be ascertained using a LED pulser attached to the TPC. This pulser can emit monochromatic light into the TPC and by operating it on very low intensity it is possible to generate single photon events. This section introduces the LED-gain-calibration on a dual phase TPC, explains its working principle and the resulting gain for each PMT is shown.

3.1 Operating principle of a PMT

Photomultipliers (PMTs) are detectors for light at ultraviolet, visible and near-infrared wavelengths that are able to detect photons even at very low count rates. The fact that a PMT can detect single photons and provide a measurable electronic signal makes it useful for many application areas in nuclear- and particle physics or even in medical fields, for example in the analysis of blood samples.

A PMT at its core is basically a chain of dynodes each of which multiplies the incident photoelectron to a larger number of photoelectrons. Figure 3.1 shows a simplified sketch of the structure of a PMT. When a photon enters the detector through the input window and reaches the cathode, it excites an electron which is emitted and attracted towards the focusing electrode from where it gets to the first dynode. On impact at the dynodes each electron generates several secondary electrons, which follow the secondary electrons from previous dynodes and produce an avalanche of electrons. After the last dynode the current is enhanced by orders of magnitude around the scale of 10^6 and is collected by the anode. At the anode the avalanche causes the potential to drop, which can be measured as a signal output.

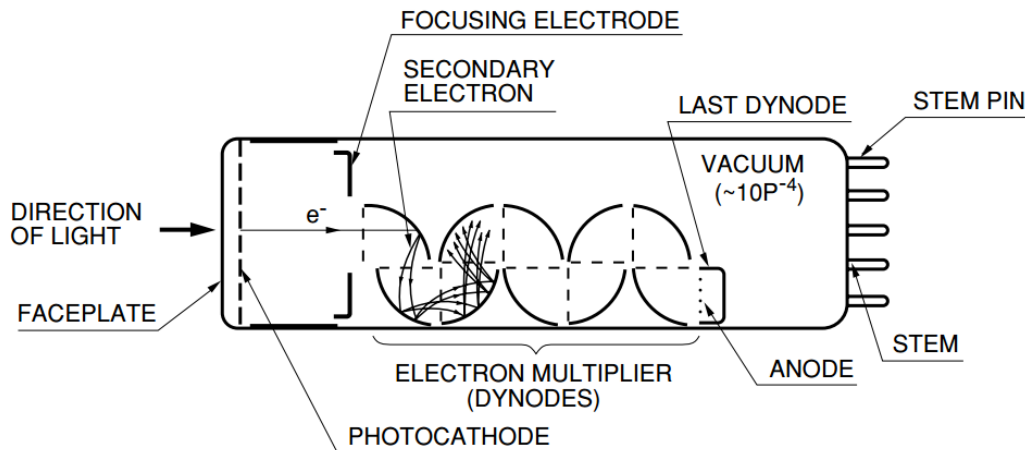


Figure 3.1: Sketch of a PMT illustrating the enhancement process of an incident photon. A photon reaching the photocathode leads to an emitted electron which gets attracted by the anode and thereby accelerated towards the dynodes. In each dynode each electron gets multiplied as secondary electrons are emitted on impact. This repeats for each dynode until an avalanche of electrons reaches the anode where they cause a potential drop as a measurable signal [13]

A PMT can be defined by two crucial values: First one is the quantum efficiency QE . It describes the number of primary photoelectrons emitted from the cathode N_{ce} for every incident photon of a certain wavelength $N_p(\lambda)$:

$$QE(\lambda) = \frac{N_{ce}}{N_p(\lambda)}. \quad (3.1)$$

The quantum efficiency is dependent on the wavelength of light. As an reminder, the *Hammatsu R8520-06-AL* PMTs, which are used here, have a QE of up to 30% for a wavelength of 178 nm (see 2.1).

The second crucial value is the gain of the PMT. The gain describes the total amplification of a single photoelectron in terms of secondary electrons N_{se} . A PMT is expected to enhance the signal of a single photoelectron by around six orders of magnitude, but the exact value differs from model to model and even between PMTs of the same model. Since approximately the incident photon only excites one electron at the cathode at all times, the gain can be calculated by dividing the charge of the output-signal Q by the charge of a single electron e , which is the input signal:

$$\text{gain} = N_{se} = \frac{Q}{e}. \quad (3.2)$$

At this point one can already see, that it is possible to assume no dependency between the gain and the photon wavelength. Therefore it is possible to calibrate the PMTs with a wavelength of choice without compromise, as long as it is able to provide enough energy for a photoeffect. Further the gain of a PMT can be influenced by the voltage applied to it. The dependency is described by

$$\text{gain} = A \cdot V^{kn}, \quad (3.3)$$

with A describing the efficiency of the dynodes to produce secondary photoelectrons, the high voltage V , a constant k that is dependent on the structure and material of the dynodes and the number of dynodes n (here $n = 10$). It is possible that photons reach the first dynode without emitting a electron at the cathode. Thereby the primary photoelectron will only be emitted inside the first dynode and for that reason lose a layer of amplification. This leads to measured gains, which are less by an order of magnitude.

3.2 Introduction to LED gain calibration

For the analysis of data created by the *Muenster xenon TPC* with *PAX* it is necessary to know the exact gain for each PMT. As mentioned in previous sections the gain is the total amplification of a single photoelectron, induced by a single photon. Therefore a method has to be chosen to ensure a single photon reaching a PMT and measure the resulting charge of the corresponding PMT output. At the *Muenster xenon TPC* this gets realized by a UV LED pulser, which is connected to the top of the TPC via a fiberglass. As the cable enters the TPC from the top, the bottom PMTs are expected to see slightly more photons than the top PMTs, as they rely on the reflections from the PTFE structure. The LED pulser gets driven by an external trigger. It gets switched on for 10 ns after the trigger signal which gets produced at a rate of 100 kHz. The idea behind this method is to run the LED pulser at low intensity, so that only few photons get emitted. In this case the amount of photons that reach a PMT corresponds to a Poisson distribution

$$P_{\lambda}(k) = \frac{\lambda^k}{k!} e^{-\lambda} \quad (3.4)$$

which describes the probability of a certain event k , with an expectation value λ . The intensity gets lowered to a point, where in 95% of cases no photon reaches a PMT, 5% of cases will have a single photon while in 0.1% two photons reach a PMT. An intensity between 5.5 V and 5.7 V for the LED was found to give a good approximation to the desired amount of single pe events depending on the position of each PMT. The distribution between the events

got approximated in a series of tests and will be examined for its suitability. In practice this leads to waveforms as the one example shown in figure 3.2. The LED is switched on

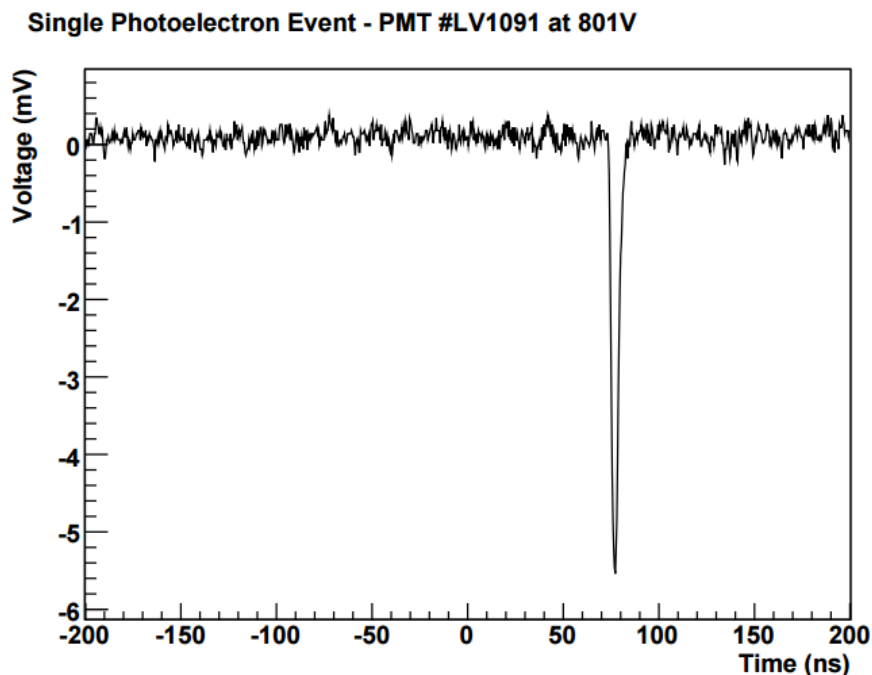


Figure 3.2: Example of a waveform where a single pe event candidate is shown. The zero point on the time scale is defined by the trigger [4].

after 50 samples (500 ns) so that the average ADC value of the samples can be defined as the baseline. It is expected that the data acquisition will see the baseline at around 16000 ADC units. This baseline then is subtracted from every sample so that a new baseline can be considered at zero. The peaks are negative because an incident photon causes a potential drop at the cathode. As the next step a window gets defined inside the waveform to isolate a peak. The window gets placed onto the next six samples anytime the LED gets triggered, so there is a 5% probability to include a single-pe peak. The range of the window was chosen to be six samples so the whole peak would be covered for certain. At the same time the window chosen should not be too wide, since this would increase the probability of catching multi pe peaks. The charge of the peak can be acquired by integrating over the voltage in the waveform section as follows:

$$Q = \int_{t_i}^{t_f} \frac{U(t)}{R} dx, \quad (3.5)$$

where in this case t_i and t_f are the initial and the final time stamp of the chosen window, $U(t)$ is the voltage at a certain time and R the impedance of the input channel of the FADC, so here for *CAEN V1724*, $R=50 \Omega$. Since the data acquisition works by analyzing a sample

over an interval of 10 ns the integral can be transformed to a sum of rectangles with the height $U(s)/R$ and the width $\Delta s = 10$ ns:

$$Q = \sum_{s_i}^{s_f} \frac{U(s)}{R} \Delta s, \quad (3.6)$$

with the initial and final sample s_i and s_f . The voltage now refers to a certain sample instead of a time unit. In this thesis the integration window will always contain the six samples from sample 256 to sample 262 corresponding to the interval from 2560 ns to 2620 ns.

With the known charge Q of a peak it is now possible to calculate the gain by using equation 3.2. Plotting the gain leads to a characteristic histogram for gain calibration as demonstrated by the idealized example in figure 3.3. The peaks in the histogram are not perfectly sharp but

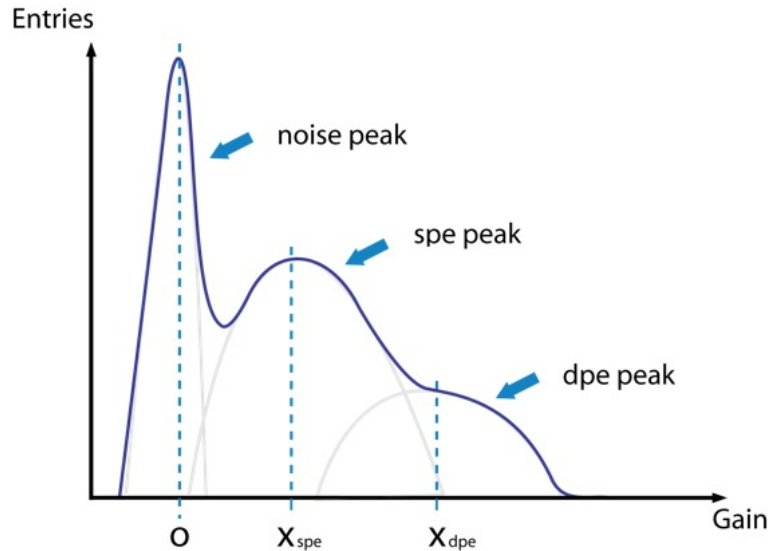


Figure 3.3: Sketch of an idealized histogram of a LED gain calibration. The histogram consists of a noise peak at zero N_{se} , a much smaller single-pe peak at x_{spe} and an even smaller double-pe peak at x_{dpe} . The mean of the dpe-peak is always double the value of the spe-peaks mean.

follow normal distribution due to the statistic process inside the dynodes of the PMT. The histogram always shows a noise peak at zero N_{ns} that is the largest peak in the histogram, often by one or several orders of magnitudes. The noise peak results from the low LED intensity since in 95% of events no pe peak is in the window. The baseline subtraction places the peaks mean at zero N_{se} , but it still reaches into positive and negative values, because of random background fluctuations. The single photoelectron (spe) peak is expected as the first peak to the right of the noise peak. The mean of the spe peak x_{spe} is the value of

interest, as it is equal to the gain. The double photoelectron (dpe) peak on the right side of the histogram appears in almost all histograms and its mean has to be double the value of the spe peaks mean. With high enough statistics or at too high intensities on the PMT, multi pe peaks will also appear with decreasing amplitudes on the higher gain values of the histogram, as the mean of the n -th multi pe peak is equal to n times the spe mean.

The program *ROOT* is used to generate the histograms for the acquired data. The data gets fitted using the *TMinuit* class of *ROOT*. *TMinuit* works by searching for the set of parameters that provides the lowest value of χ^2 (total difference between fitting function and data) for the fit.

3.3 LED gain calibration

The data points result in a histogram, which shows at least two characteristic peaks, the noise peak and the spe peak. The LED gain calibration is demonstrated at the histogram of PMT2. The data got taken with 5.5 V applied to the LED, while the TPC ran in dual phase mode with electric fields switched on. PMT2 belongs to the outer PMTs at the bottom of the TPC. The histogram after applying the steps explained in chapter 3.2 for 10^6 events at a rate of 100 kHz is shown in figure 3.4. The x-axis shows the gain (gain= N_{se}) and the y-axis the number of corresponding events. All following histograms are plotted with 70 bins, to ensure enough counts in each single bin, especially for higher gains. It is intended to have a minimum of ten events in every single bin for the range of the fit that is intended to be from $-1 \times 10^6 N_{se}$ to $10 \times 10^6 N_{se}$ to cover a large part of the noise peak and also the double- or a triple pe peak (if necessary). In reality the peaks are not perfectly sharp and often even overlap. Therefore the position of the second largest maximum is not automatically the spe-mean and therefore the actual gain. The peaks have to be fitted with the sum of multiple Gaussians, also known as a *single electron response* (SER) function.

3.3.1 Single photoelectron peak fit

The basic approach to fitting this histogram is to assume only a small influence by multi pe peaks on the spe-mean. Therefore only one Gaussian summand for each peak (the noise peak and the spe peak) gets applied resulting in

$$g_2(x) = A_n \cdot e^{\left(-\frac{1}{2} \frac{x-x_n}{\sigma_n}\right)^2} + A_{spe} \cdot e^{\left(-\frac{1}{2} \frac{x-x_{spe}}{\sigma_{spe}}\right)^2} \quad (3.7)$$

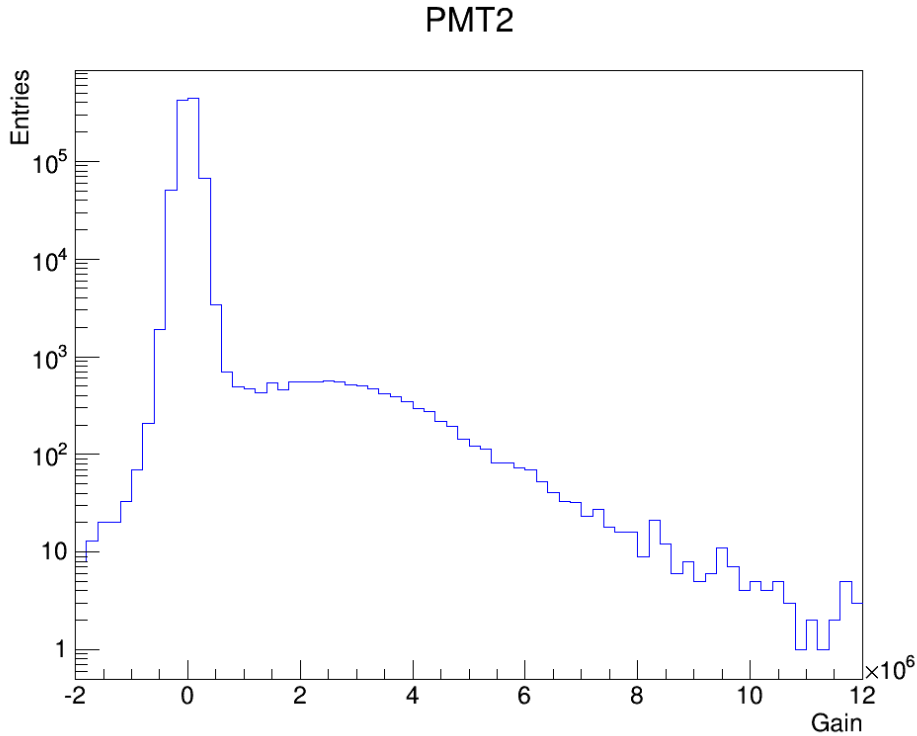


Figure 3.4: Histogram produced with data from PMT2. The x-axis consists of 70 bins.

for the SER-funktion. A_i is the amplitude for each Gaussian, x_i is the mean and σ_i the standard deviation. The mean of the noise peak can be set to $x_n = 0$ to decrease the number of free parameters for the problem by one, leaving five. Figure 3.5 shows the resulting fit from applying $g_2(x)$ to the one million events of PMT2 in the range from 0 to 10×10^6 .

As already mentioned the overall fit is not supposed to cover the entire histogram. The noise peak is important, but increasing the range to negative values past the noise peak is not reasonable as the spe peak then appears as a dominant function although negative gains are unphysical. In this case the fit even starts at zero since the noise peak is sharp compared to other histograms. Also the range should not reach values where the data is not covered by sufficient statistic as mentioned above. In any case the individual Gaussians for each peak are drawn across the whole range of the histogram, to make the overall fit easier to understand. In figure 3.5 the fit seems to describe the problem, but has obvious flaws that can be easily shown by analyzing the spots where the fitting function differs from the actual data (an detailed analysis of the residuals for each fit is omitted at this point since this is for demonstration purposes only, but can be seen in the appendix): The valley between noise- and spe peak is not described by the fit, same for the data around the spe peak and especially past 7×10^6 N_{se} , resulting in a $\chi_{red}^2 = 5.00$ at $70 - 5 = 65$ NDF (number of degrees of freedom) when $\chi_{red}^2 \approx 1$ is desired. Additionally it is worth mentioning that every number of entries

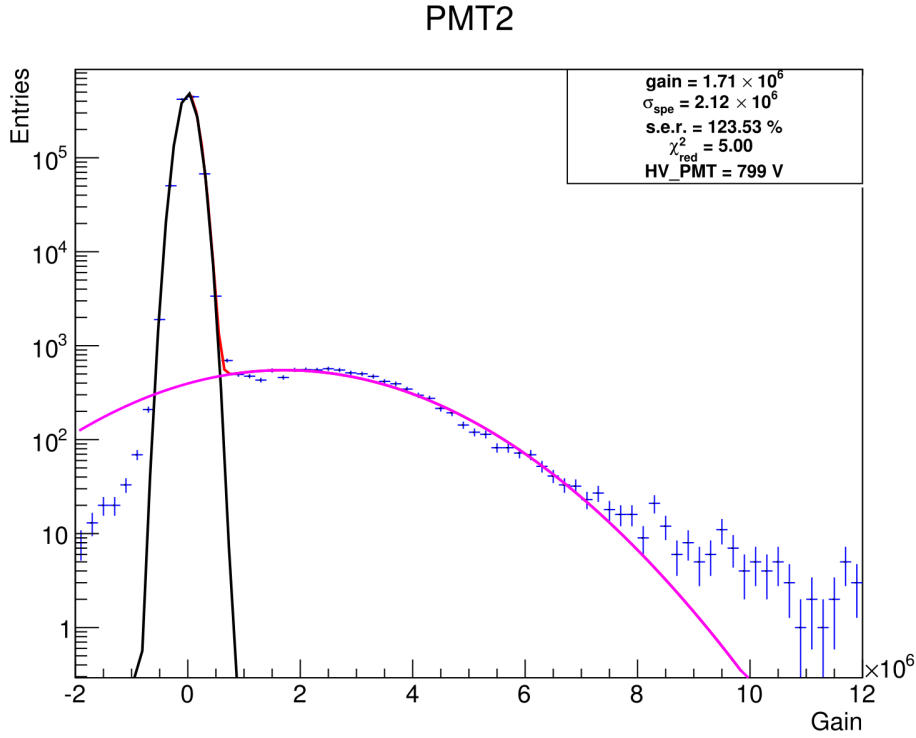


Figure 3.5: PMT2 histogram with two Gaussians fitted. The black line shows the noise peak, the pink one shows the spe peak. The red line shows $g_2(x)$.

N in a bin is linked to an error of \sqrt{N} due to Poisson distribution. However it occurred that the large, and therefore well determined noise peak can still show differences between fit and data due to its low relative error. This is not visible in the plot since the y-axis is in logarithmic scale, but appears when analyzing the residuals. To compensate for the deviation at the noise peak and to emphasize the quality of the fit towards the pe peaks, the error for each bin i got changed to

$$\Delta N_i = \sqrt{N_i + x^2 N_i^2}, \quad (3.8)$$

where x is a percentage error that can be set depending on the deviation around the noise peak. For small N , the error converges to \sqrt{N} and for large N to $x \cdot N$, therefore reducing the noise peaks impact on the χ^2 by increasing the error for bins with high entries. In the following x got set between 3% and 5% for each PMT individually, with the aim of reducing the noise peaks influence as much as possible without influencing the other peaks. For PMT2 $x = 5\%$ was sufficient.

3.3.2 Double and triple photoelectron peak fit

To improve the quality of the fit, another Gaussian gets added to the fitting function to take a double pe peak into account. As explained above, the mean of the dpe peak gets predefined as double the spe peak

$$x_{dpe} = 2x_{spe}. \quad (3.9)$$

Also the widths of the peaks are linked by Gaussian statistic like

$$\sigma_{dpe} = \sqrt{2}\sigma_{spe}. \quad (3.10)$$

With these constrains only one new free parameter has to be implemented into $g_2(x)$ resulting in the new fitting function

$$g_3(x) = A_n \cdot e^{\left(-\frac{1}{2} \frac{x}{\sigma_n}\right)^2} + A_{spe} \cdot e^{\left(-\frac{1}{2} \frac{x-x_{spe}}{\sigma_{spe}}\right)^2} + A_{dpe} \cdot e^{\left(-\frac{1}{4} \frac{x-2x_{spe}}{\sigma_{spe}}\right)^2}, \quad (3.11)$$

with the amplitude of the dpe peak A_{dpe} . The result of applying the fit to the data of PMT2 is shown in figure 3.6. Figure 3.6 shows that the fitting function describes gains beyond the

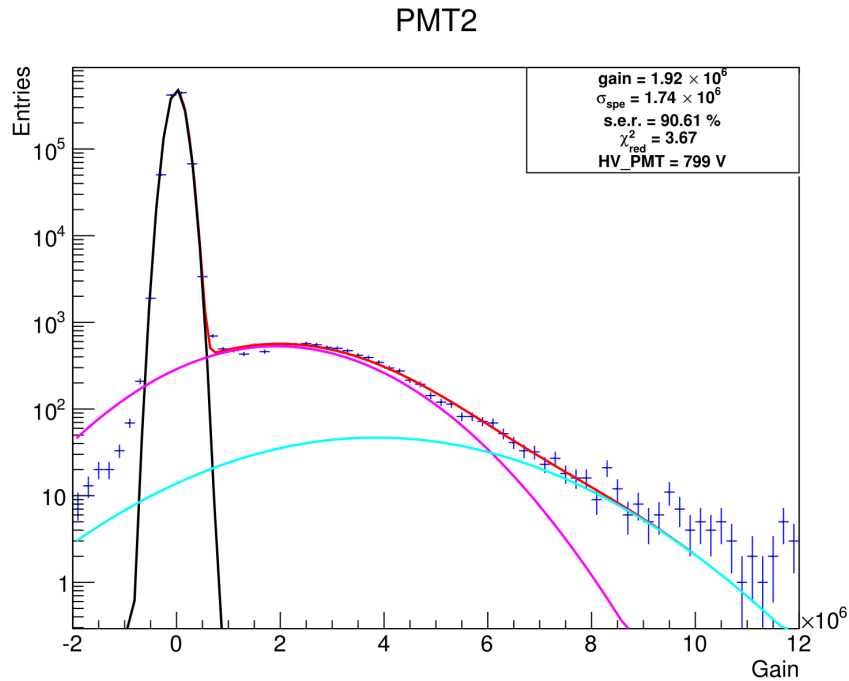


Figure 3.6: PMT2 histogram with three Gaussians fitted. As before, the black line shows the noise peak and the pink one shows the spe peak. The dpe peak is visualized by the cyan line. In this case the dpe peak already causes the spe mean (and so the gain) to shift. The region beyond $3 \times 10^6 N_{se}$ now gets described better.

noise peak better than before. Also already visible is an improvement of χ_{red}^2 towards 1. Still problematic is the valley, where the fit does not describe the data well. At this point the so called dynode Gaussian gets applied to the fit. The dynode Gaussian is seemingly another noise peak centered around zero N_{se} but much smaller as the actual noise peak. The dynode Gaussian originates from photons entering the dynodes inside a PMT without emitting a pe at the cathode beforehand as already mentioned. The mean of the dynode Gaussian is expected at close to zero but can vary as its mean is one less order of magnitude due to the missed layer of amplification compared to a regular pe. Adding the dynode Gaussian with three new free parameters to the fitting function leads to

$$g_4(x) = A_n \cdot e^{\left(-\frac{1}{2} \frac{x}{\sigma_n}\right)^2} + A_{dyn} \cdot e^{\left(-\frac{1}{2} \frac{x-x_{dyn}}{\sigma_{dyn}}\right)^2} + A_{spe} \cdot e^{\left(-\frac{1}{2} \frac{x-x_{spe}}{\sigma_{spe}}\right)^2} + A_{dpe} \cdot e^{\left(-\frac{1}{4} \frac{x-2x_{spe}}{\sigma_{spe}}\right)^2}. \quad (3.12)$$

Using $g_4(x)$ to fit the data of PMT2 is pictured in figure 3.7. The gain of PMT2 can already

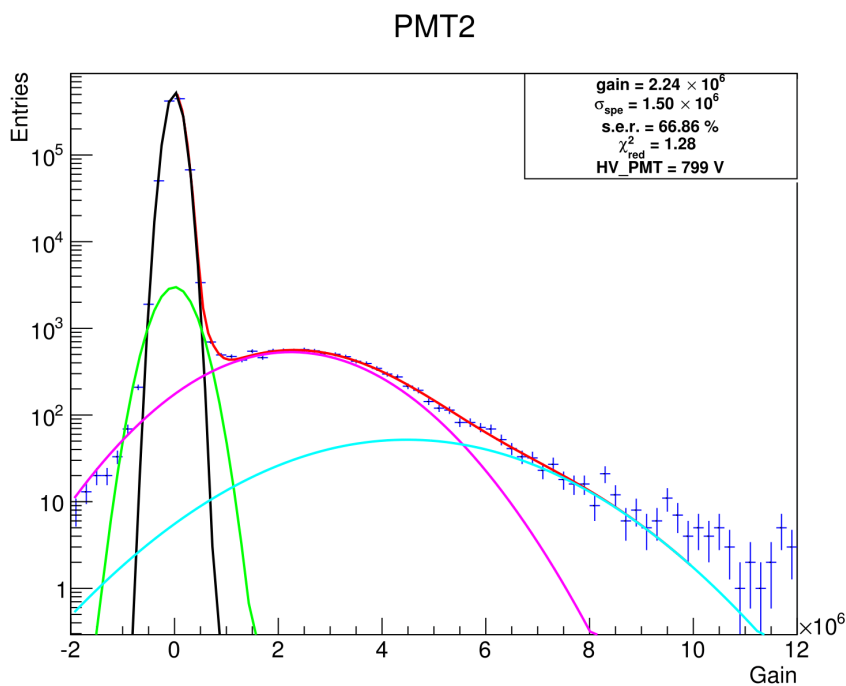


Figure 3.7: PMT2 histogram with four Gaussians fitted. The dynode Gaussian is visualized by the green line. Due to the presence of the dynode Gaussian the spe peak (and therefore also the dpe peak) got more narrow, allowing for a proper description of the valley. The fit describes the data better, according to its $\chi_{red}^2 = 1.28$.

be read out of figure 3.7 as the χ_{red}^2 gets another step closer to 1. To improve the fit even

more for the present problem, a triple photoelectron (tpe) Gaussian gets added to the fitting function. The mean of the tpe peak is again depended on the spe mean, this time by

$$x_{tpe} = 3x_{spe}. \quad (3.13)$$

Just as for the dpe peak, the widths are correlated as well:

$$\sigma_{tpe} = \sqrt{3}\sigma_{spe}. \quad (3.14)$$

Therefore the tpe peak can be added again while only adding the one new free parameter A_{tpe} , the tpe amplitude, to the fitting function, to a total of ten free parameters:

$$\begin{aligned} g_4(x) = & A_n \cdot e^{\left(-\frac{1}{2} \frac{x}{\sigma_n}\right)^2} + A_{dyn} \cdot e^{\left(-\frac{1}{2} \frac{x-x_{dyn}}{\sigma_{dyn}}\right)^2} \\ & + A_{spe} \cdot e^{\left(-\frac{1}{2} \frac{x-x_{spe}}{\sigma_{spe}}\right)^2} + A_{dpe} \cdot e^{\left(-\frac{1}{4} \frac{x-2x_{spe}}{\sigma_{spe}}\right)^2} \\ & + A_{tpe} \cdot e^{\left(-\frac{1}{6} \frac{x-3x_{spe}}{\sigma_{spe}}\right)^2}. \end{aligned} \quad (3.15)$$

It has to be stated, that the tpe peak is not absolutely required in this special case, since at the range, where the dpe peak stops describing the data, already the entries are not higher than 10 per bin. Also a tpe peak would not even be necessary if the desired ratio of no events in 95% of cases, spe events in 5% and dpe events in 0.1% would have been achieved perfectly. Therefore the presence of the tpe peak is a sign for a too high intensity at the LED pulser. Regardless, the completed fit is shown in figure 3.8. Since the χ_{red}^2 decreased again it can be stated that the fit improved another time by adding a tpe Gaussian to the fitting function. Also figure 3.8 shows a plot of the fits normalized residuals, calculated for each bin i using

$$\text{res}(i) = \frac{y_i - g_5(x_i)}{\Delta N_i}. \quad (3.16)$$

A look onto the normalized residuals shows that the overlap between actual and second noise peak does not solve the problem around the noise peak completely. Also there happen to be oscillations in the residuals from around $2 \times 10^6 N_{se}$ on, that get larger the less statistic is in each bin. This indicates that there are systematical problems with the chosen fitting function and has to be analyzed in future work.

3.3.3 Results of the LED gain calibration

Using function $g_5(x)$ while setting reasonable start parameters and parameter limits allows a gain calibration for every PMT. The fitted histograms can be seen in the appendix. Table

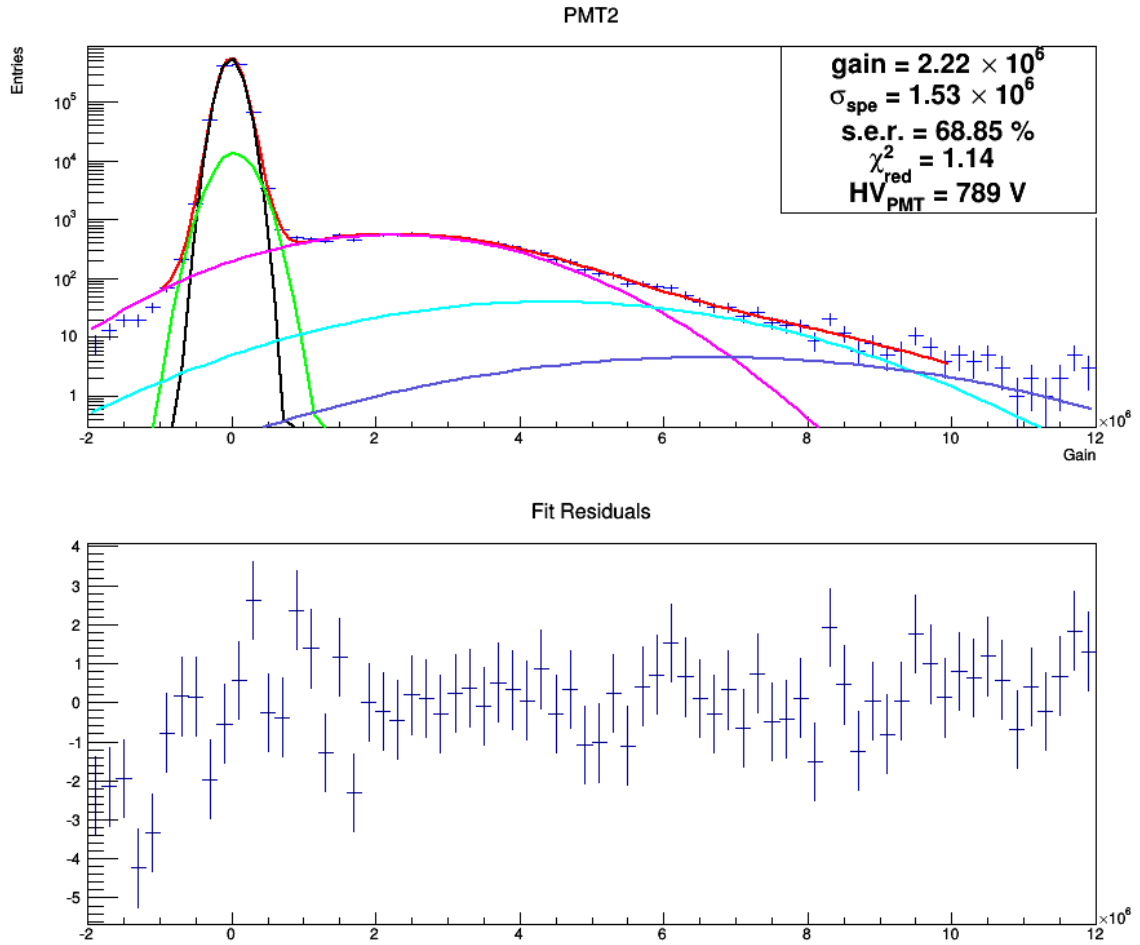


Figure 3.8: Histogram of the data collected at PMT2 and fitted with $g_5(x)$. The blue line shows the newly added tpe peak. Additionally the residuals for the fit are plotted below the histogram. As can be seen the noise peak still leads to high (absolute) residuals. The area around the spe mean gets described well with slight fluctuations in the residuals leading to the assumption that the dpe- and tpe peak are not described perfectly by the Gaussian distribution maybe due to not sufficient statistics. The final fit parameters are shown in the appendix.

3.1 shows the results of all 14 PMTs, except PMT5, that was affected by serious technical problems at the time the data was taken, to the point where it was impossible to analyze it using this method. Also shown is the *single electron resolution* (s.e.r.), given by

$$\text{s.e.r.} = \frac{\sigma_{spe}}{x_{spe}}, \quad (3.17)$$

for upcoming further analysis of the PMTs. The error for the gain is given by the parameter error of $ROOT$. The results presented in table 3.1 ensue from the fitted histograms that are shown in the appendix with their fit parameters.

Table 3.1: Results for each PMTs gain and single electron resolution

PMT	gain $\times 10^6$	s.e.r	PMT	gain $\times 10^6$	s.e.r.
0	2.05 \pm 0.04	106.60%	7	2.07 \pm 0.09	83.89%
1	2.06 \pm 0.04	102.90%	8	2.39 \pm 0.02	83.60%
2	2.22 \pm 0.04	68.85%	9	2.88 \pm 0.03	63.50%
3	2.48 \pm 0.04	55.68%	10	1.43 \pm 0.12	195.59%
4	3.37 \pm 0.12	77.15%	11	2.61 \pm 0.03	67.40%
5	-	-	12	2.45 \pm 0.04	85.40%
6	2.02 \pm 0.09	122.96%	13	2.42 \pm 0.05	80.41%

3.3.4 Comparing the measured events to the expectations from Poisson statistic

Assuming that the count rates for spe- and dpe- events are all Poisson distributed, the areas of the peaks can be constrained to another in order to compare the results of the fits to the expectations. First, the average number of of a k -pe (k = number of detected pe) event happening is set to μ . Therefore the probability P of a k -event happening results in

$$P_k(\mu) = \frac{\mu^k}{k!} e^{-\mu}. \quad (3.18)$$

Based on this, it can be seen that the ratio between single ($k = 1$) and double ($k = 2$) event-probability is constant at all cases:

$$\frac{P_2(\mu)}{P_1(\mu)} = \frac{\mu^2}{2!} \frac{1! e^{-\mu}}{\mu e^{-\mu}} = \frac{\mu}{2} = \text{const.} \quad (3.19)$$

Here μ is the expectation value of a k -event happening. Since the desired distribution of 95%/5%/0.1% for the k -events was only estimated for each PMT, a constant μ for all PMTs is not expected. Therefore P_2/P_1 is plotted against $F_1 + F_2$ (with F_k being the area of the k -pe Gaussian) to compare $\mu/2$ for each PMT with the total amount of events the PMT has seen. If the PMT has detected more events in total compared to another PMT, a higher amount of multi-pe peaks is expected and therefore a higher μ . A conclusion is, that P_2/P_1 plotted against $F_1 + F_2$ for all PMTs is expected to have a linear behavior. Since P_2 and P_1 are unknown on their own, the ratio between the probabilities P_2 and P_1 gets expressed through the ratio between F_2 and F_1 :

$$\frac{P_2}{P_1} = \frac{F_2}{F_1}. \quad (3.20)$$

The results are shown in figure 3.9.

The expected linear correlation for the ratio of the areas to the total area is not visible

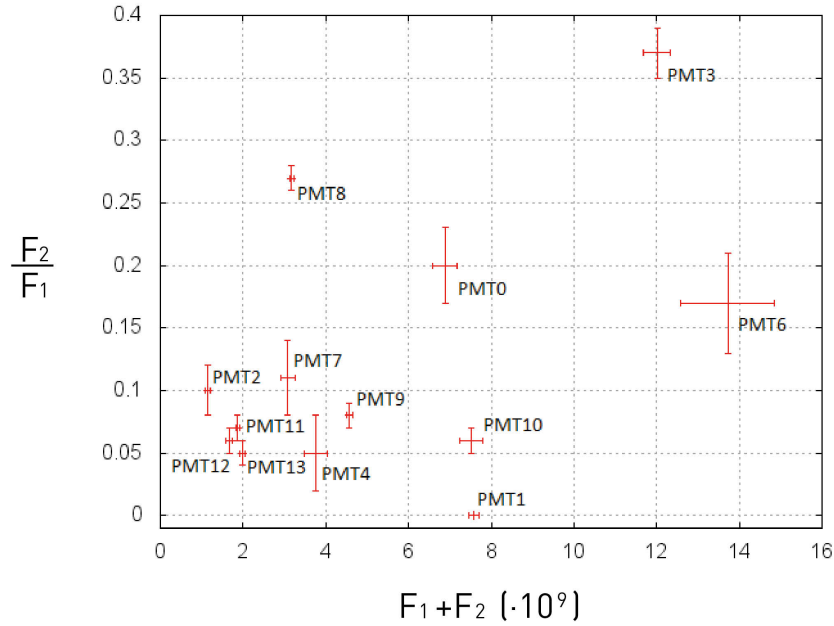


Figure 3.9: The ratio between the area of the spe peak and the dpe peak for all PMTs plotted against the sum of both.

in figure 3.9. This has various reasons. For one, the high voltage of the PMTs impacts the gain. PMT3 for example has a large tail of multi pe peaks beyond the spe- and dpe peak (see figure 3.10) and because only spe-, dpe- and tpe peak are taken into account, those are covering an area where other multi pe peaks could have an impact if they would get considered and therefore decrease the total area of spe- and dpe peak. Another thing that has to be taken into account that some PMTs receive more light due to their position inside the detector and the detector geometry. Further the LED voltage is not constant through the analysis due to the previous reason. In theory the ratio of F_2 to F_1 should be always 0.02, since it is desired to have 5% spe events and 0.1% dpe events, meaning 50 times more spe events than dpe events. This value did not get achieved for any PMT (PMT1 has no dpe peak fitted at all, therefore should not be considered here, see appendix A.2). Reaching this value for all PMTs would also presuppose that every PMT sees the exact same amount of light, which is not possible due to the geometry of the detector and the fact that with only a single LED pulser the light will always have unequal intensity for some PMTs. It can also be argued that having a tpe peak fitted in only some histograms impacts the area and ratio of F_1 and F_2 , but removing all data points with not only a spe and dpe Gaussian fitted still does not show a clear linear behavior either (see figure 3.11). Two possibilities are noted by the blue and the grey line, but since there is only few statistic left, a sure conclusion is not possible.

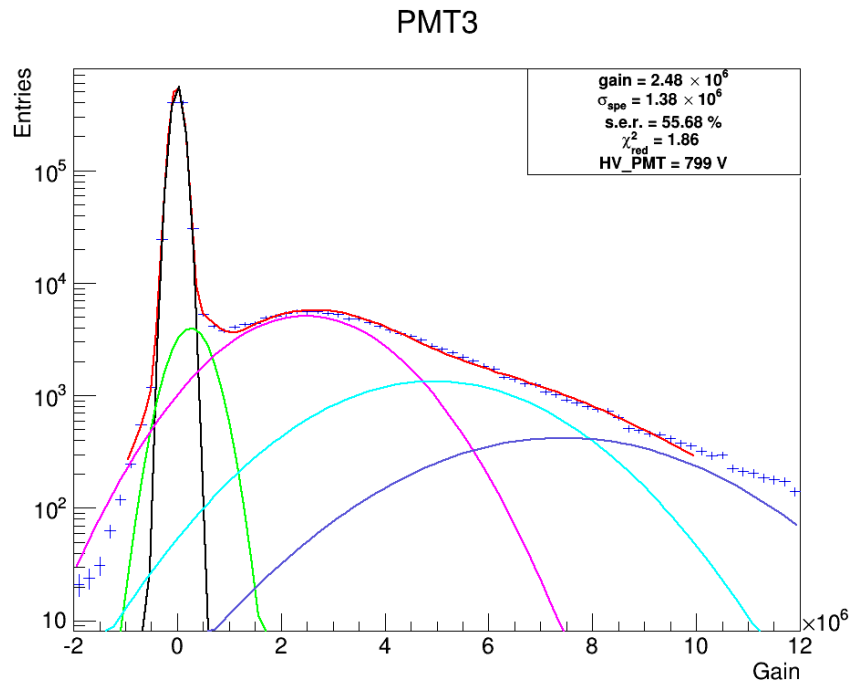


Figure 3.10: Histogram of PMT3. There are many events compared to other PMTs even at gains beyond $10 \times 10^6 N_{se}$. Therefore the spe and dpe peak cover a large area in the histogram compared to others.

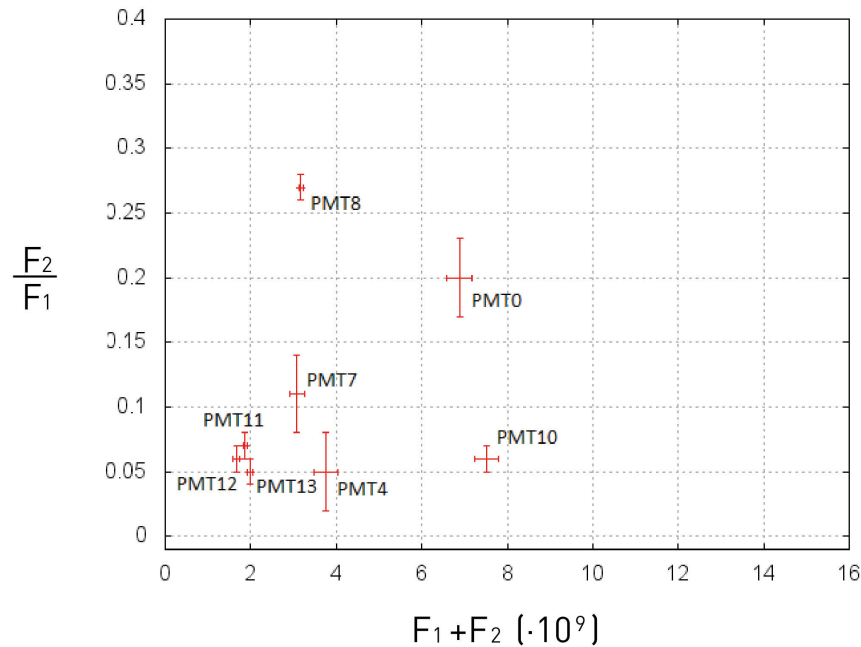


Figure 3.11: The same plot as in figure 3.9, but with all PMTs removed, that had a tpe peak included in the fitting function. PMT1 got also removed since it had no dpe peak fitted. Since there is not much statistic in the plot, it is not possible to spot a clear linear behavior although two possibilities are suggested by the blue and grey line.

4 Energy calibration

To analyze S1 and S2 signals inside the *Muenster xenon TPC* an energy calibration is required beforehand. As previously mentioned, data taken from the TPC gets processed with *PAX*, to make it usable. *PAX* gives out all important information around the data collected, as for example the intensity of a signal and where it originated from. To proportion the output of *PAX* radioactive calibration sources are used since they can induce S1 signals with known energies inside the detector. The output of *PAX*, which is given in pe-units, can then be compared to the expected energy to determine the light yield of the detector.

4.1 Preparation and measuring

For this thesis the chosen calibration source is ^{137}Cs . The ^{137}Cs beta decay causes indirectly a gamma at an energy of 662 keV. Previous simulations approaching the *Muenster xenon TPC* showed, that a ^{137}Cs source placed directly outside of the detector is able to penetrate the detection volume with a sufficient number of interactions to determine the LY of the detector [9]. The source was fastened at the outer shell of the detector and at medium height of the actual detection volume. The TPC ran in dual phase mode, with the electric fields switched on (12 kV at the cathode and 2.99 kV at the anode). Over the course of 230 min 10^6 events were taken and processed with *PAX* for further analysis. At this point the signals were not LCE corrected for the detector geometry as suggested in [9]. The measured S1 signals are shown in figure 4.1.

4.2 Analysis of the ^{137}Cs measurement

The first step that has to be done, is to eliminate unwanted data, like background noise or signals from other sources, from the data. Therefore several cuts are applied to the data and their consecutive impact on the data is shown.

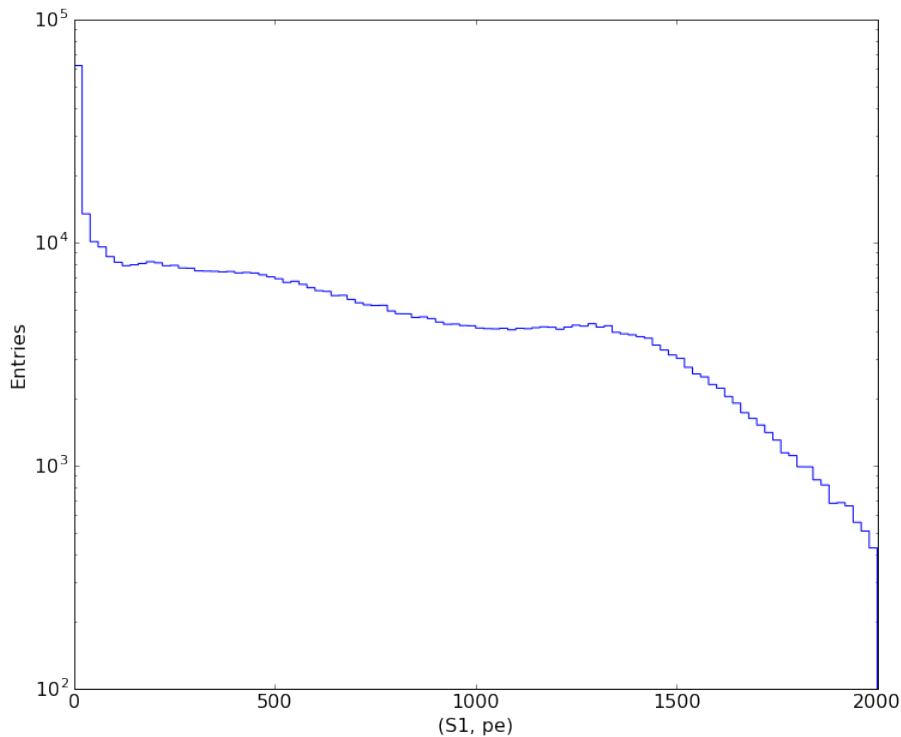


Figure 4.1: Spectrum of all measured S1 signals (without any cuts on the data).

- First, all S1 and S2 signals have to be larger than zero. Negative S1s and S2s can not originate from gammas induced by the ^{137}Cs source and are non-physical. Those should get sorted out by *PAX*, but this cut is just to be on the safe side. Further, the signals should have a minimum intensity to be physically relevant. All events that do not fit $S1 > 3$ pe and $S2 > 150$ pe get cut (53.3% of data left).
- Afterwards, the fiducial volume gets defined inside the detection volume. Events that originate in the center of the detector have the least chance of originating from other sources than ^{137}Cs . The volume near the bottom and the top of the detection volume can produce unwanted events due to the anode, cathode and the meshes that protect the PMTs. Also by reducing the volume to the center, less radiation from outside influences the results. Therefore the detection volume gets reduced to $z \in [-12, -5]$ with the top of the detection volume having $z = 0$ and the bottom having $z = -17$ (22.6% of data left after applying the cut).
- It is expected that most of the PMTs would observe a 662 keV- ^{137}Cs event, since it is a high energy signal. Therefore a cut was implemented to cut out all events that have not been seen by at least eleven PMTs, meaning only two PMTs were allowed to not see the event since PMT5 was inactive during the analysis (14.3% of data left).

- *PAX* can find S1 events that can not be matched to a S2 event. Those events are called “largest other S1”. Those events get cut from the data (7.0% of data left).

After applying the cuts 69908 events were left in the data. Since it was not possible to identify the energy of the ^{137}Cs gamma in the S2 spectrum, further analysis will be focused on the S1 spectrum after cuts (see figure 4.2). An analysis of the S1 energies is expected to show a behavior as shown in figure 2.4. However again there are no sharp peaks expected, due to the statistical behavior of the PMTs, but instead smeared out Gaussians. Therefore, and due to detector geometry it will not be possible to observe a Compton edge in the spectrum as already the previous GEANT4 Monte Carlo simulation for ^{137}Cs in [9] showed a continuous spectrum up to a large peak at 662 keV. With this in mind the largest peak in the S1 spectrum is expected to be the 662 keV-peak. Against the expectations the S1 spectrum does not show

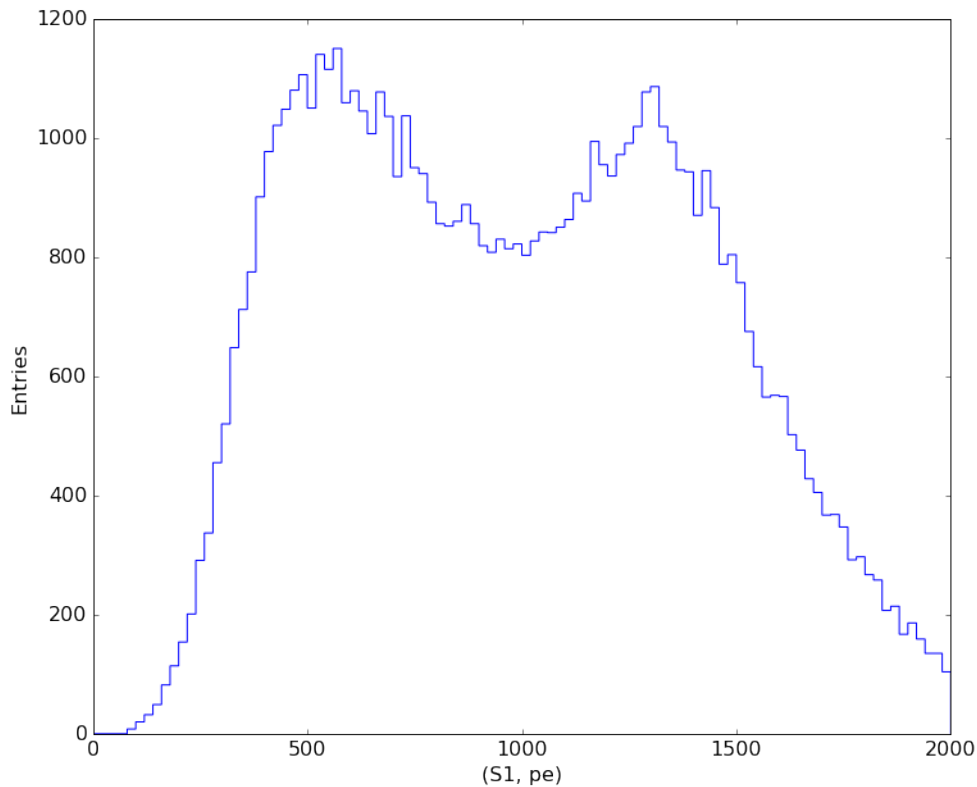


Figure 4.2: Spectrum of the S1 signals after applying all cuts. Instead of only one expected large peak there are two significant ones of similar scale.

one, but two peaks of similar height. Also the Compton spectrum in the low energy range seems to be removed by the cuts. Up to this point it can not be stated for sure which of both peaks is the 662 keV peak of ^{137}Cs , or what caused the other peak. Therefore both peaks are fitted with a Gaussian each:

$$g(x) = A_1 \cdot e^{-\frac{1}{2}\left(\frac{x-\mu_1}{\sigma_1}\right)^2} + A_2 \cdot e^{-\frac{1}{2}\left(\frac{x-\mu_2}{\sigma_2}\right)^2}. \quad (4.1)$$

The mean μ_i of one of the Gaussians is then equivalent to an energy of 662 keV. Figure 4.3 shows the S1 spectrum with the double Gaussian fitted. The double Gaussian seems to not

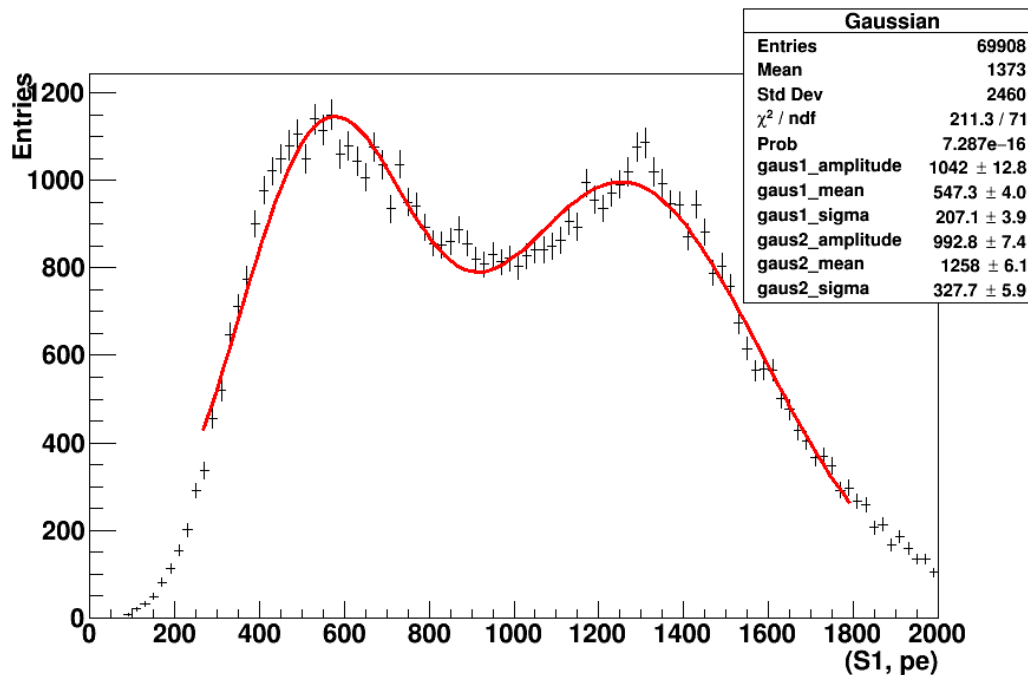


Figure 4.3: Spectrum of S1 signals with the Gaussians fitted around the two largest peaks. The fit is not representing the data in a very good way, but gives an idea that more than one signal is included in the spectrum. The mean of one of the Gaussians in pe units is equivalent to an energy of 662 keV.

be quite sufficient to describe the data alone, but gives the general idea that more than just one signal is included in the spectrum. The following parameters are obtained by the fit:

- A_1 : 1024.82 ± 13.70
- μ_1 : (541.33 ± 3.32) pe
- σ_1 : (185.24 ± 2.69) pe
- A_2 : 992.84 ± 7.36
- μ_2 : (1257.65 ± 6.11) pe
- σ_2 : (327.74 ± 5.89) pe

The light yield can now be calculated for each peak:

$$\text{LY}_1 = \frac{\mu_1 \text{ pe}}{662 \text{ keV}} = (0.82 \pm 0.01) \frac{\text{pe}}{\text{keV}}, \quad (4.2)$$

$$\text{LY}_2 = \frac{\mu_2 \text{ pe}}{662 \text{ keV}} = (1.90 \pm 0.01) \frac{\text{pe}}{\text{keV}}. \quad (4.3)$$

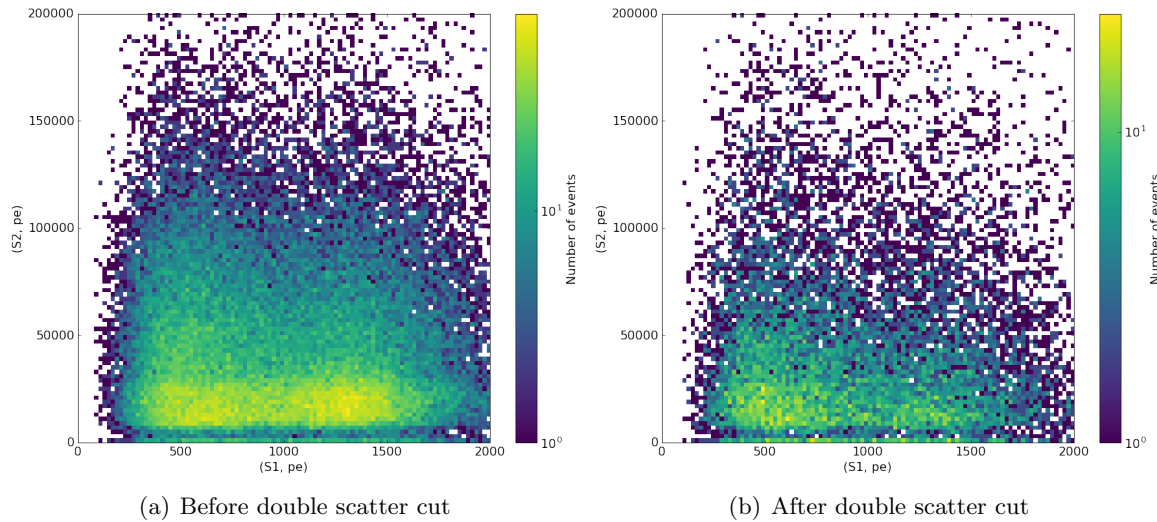


Figure 4.4: Spectrum of S1 and S2 before and after the double scatter cut. Before the cut, there are two peaks visible, with the right one being slightly stronger. After the cut the right peak seems to be almost vanished, while the left one is still clearly visible.

Also the energy resolution $\Delta E/E$ of the detector can be determined for both peaks. The energy resolution is a characteristic value for scintillation detectors and describes the minimal distance two peaks can have for the detector to still identify them as two separate peaks. It is defined as the ratio of a peaks standard deviation to its height:

$$\frac{\Delta E_1}{E_1} = \frac{\sigma_1}{\mu_1} = (34.22 \pm 0.01)\%, \quad (4.4)$$

$$\frac{\Delta E_2}{E_2} = \frac{\sigma_2}{\mu_2} = (26.06 \pm 0.01)\%. \quad (4.5)$$

The energy resolution suffers from the two large peaks being in close vicinity to each other. To further investigate which of both peaks is the 662 keV a double scatter cut is implemented. It is possible that one of the peaks consists of a large number of events, which have two large peaks in a very short time frame, that are identified by *PAX* as two peaks but originate from a double scatter, it is not of interest for this analysis since a double scatter would imply double the amount of energy deposited in the detector. An example for a perfectly matched S1-S2 event can be found in the appendix in A.3.

To remove the double scatter events, a pragmatic way is chosen: a condition was set, that the energy of the closest peak to the looked at S2 (“largest other S2”) must only be 0.01% of the actual S2 at maximum (now 1.8% of all data left). Figure 4.4 compares the S1-S2 spectrum before and after the cut. Before the cuts there are two peaks visible in the spectrum, as they were already discussed in the S1-only spectrum. While decreasing the allowed size of the largest other S2 up to 0.01% of the actual S2 it can be observed, that the right peak in the

spectrum disappears much faster than the left one. The spectrum in figure 4.6 shows still a clear peak around 513 pe while the other peak decreased to now only half the amplitude of the first peak. This suggests that the first peak is the real ^{137}Cs peak at 662 keV. The other peak might then originate from *PAX* not being able to identify events with double scattered S2s properly. The S1 spectrum will get fitted again, the result is shown in figure 4.5. The

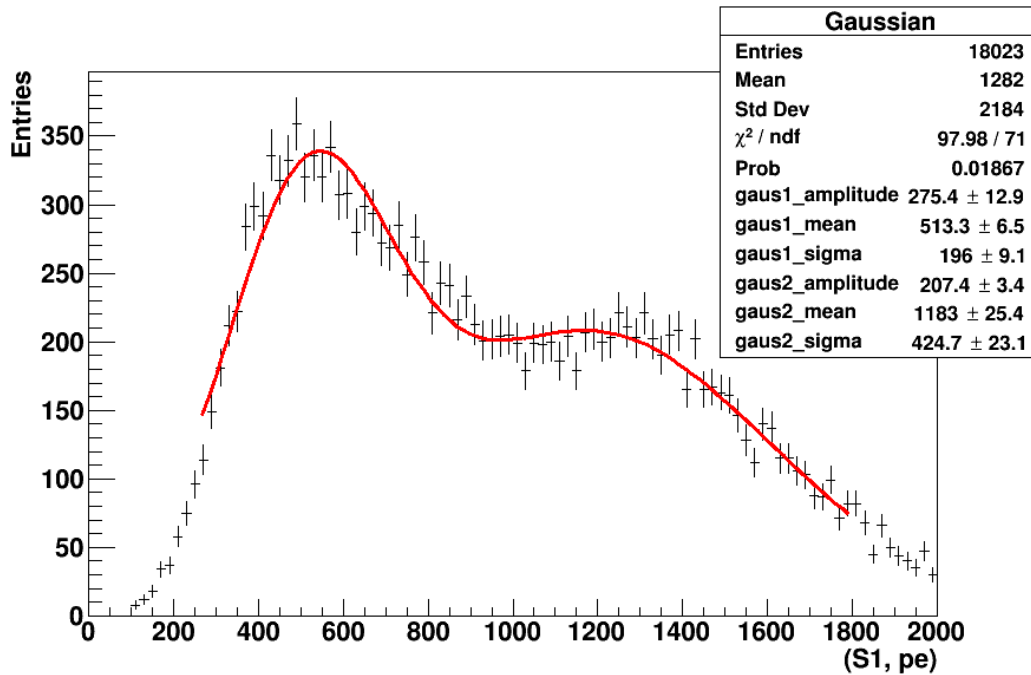


Figure 4.5: Spectrum of S1 after the double scatter cut with the same fit applied as beforehand. The peak on the right lost much more on size compared to the peak on the left, which is now assumed to be the 662 keV peak.

new fitting parameters are:

- A_1 : 275.36 ± 12.91
- μ_1 : (513.35 ± 6.46) pe
- σ_1 : (195.97 ± 9.12) pe
- A_2 : 207.41 ± 3.38
- μ_2 : (1182.56 ± 25.42) pe
- σ_2 : (424.67 ± 23.09) pe

To get a better understanding of the data, randomly chosen events got analyzed one by one. It occurred, that *PAX* has indeed problems identifying double scatter events. The example in figure 4.6 shows a fine S1 signal (strong increase, exponential decrease) but a flawed S2 signal due to a double scatter. The S2 was merged from two peaks, because the time frame in between was not long enough for *PAX* to identify them as two independent ones. Therefore

the S2 signal gets provided with about double the charge as it should have been. This might be the reason for the failed reconstruction of S1-S2-events. At the *Muenster xenon TPC*

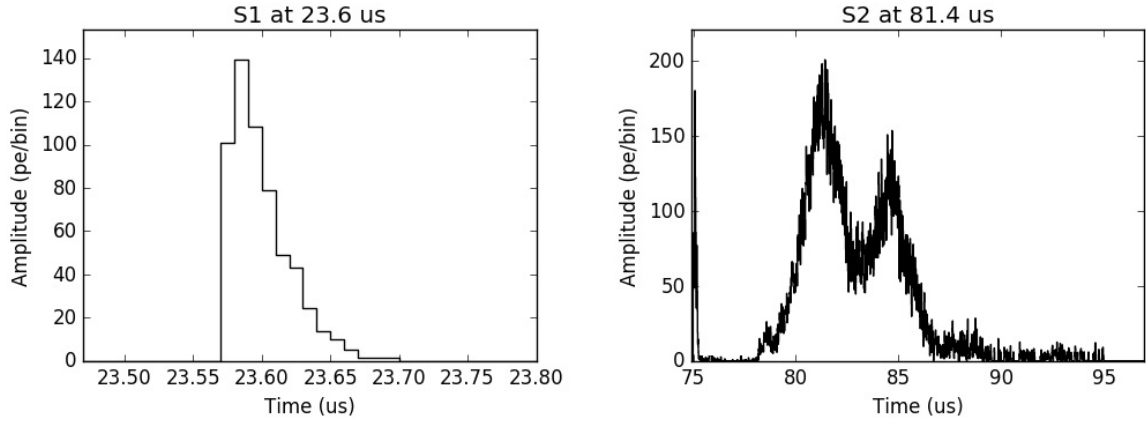


Figure 4.6: Example for an event with a fine S1 signal (left), but a double scatter S2 (right). *PAX* only identified a single S2 peak, that is merged from the two actual peaks due to the short time frame in which both occurred. Therefore the S2 signal is provided with about double the real charge, which is of course a false information that needs to be cut out of the data.

PAX never got calibrated to identify those kinds of double scatters as independent peaks. This could be a future task to improve the quality of the measured data.

The light yield and the energy resolution are now only calculated for the large peak:

$$LY_1 = \frac{\mu_1 \text{ pe}}{662 \text{ keV}} = (0.78 \pm 0.01) \frac{\text{pe}}{\text{keV}}, \quad (4.6)$$

$$\frac{\Delta E_1}{E_1} = \frac{\sigma_1}{\mu_1} = (38.17 \pm 0.01)\%. \quad (4.7)$$

Both the light yield and the energy resolution deteriorated a bit. For comparison: the energy resolution of the XENON100 detector for S1 signals is around 12.5% [2]. Although the energy resolution was not expected to be as good as the one from XENON100, a large difference shows up here, due to many reasons. The XENON100 detector has 178 PMTs [2] that have been under constant check for years. Additionally XENON100 uses lifetime corrections and light collection efficiency corrections to make up for effects inside the detector that influence the results and thereby improve the detector's energy resolution. Those corrections could not yet get implemented at the *Muenster xenon TPC*. Additionally the energy resolution at the *Muenster xenon TPC* decreases as a result of the unknown signal in the S1 spectrum.

A Monte Carlo simulation performed for ^{83m}Kr as a calibration source performed in [9] resulted in a light yield of around 1 pe/keV. Taking into account that empirically the light yield for ^{83m}Kr tends to be slightly better than for ^{137}Cs , this also indicates that the large peak in 4.5 is indeed ^{137}Cs .

5 Conclusion and outlook

This thesis ascertained the gains for the PMTs implemented at the Muenster xenon TPC and used them to calibrate the light yield of the detector. In contrast to previous gain calibrations this one used a sum of up to five Gaussians, while taking correlations between multi pe peaks into account, to fit the collected data of each PMT individually. The light yield was to be ascertained by placing a radioactive gamma source, ^{137}Cs , near the detector so it could penetrate the detection volume and thereby produce S1 and S2 signals. Although the light yield could not be determined for certain, two possible traces of the ^{137}Cs 662 keV decay have been isolated and analyzed.

As a first step a LED pulser attached to the TPC was used to emit light at low intensity to the PMTs. The PMTs raw output in ADC units were then converted to a histogram, which shows the amount of events for a specific number of N_{se} . Having the LED at low intensity causes a large noise peak in the histogram, which is used to determine the spe peak in the histogram as the first peak to the right of the noise peak. The mean of the spe peaks Gaussian can then get identified as the gain of the investigated PMT. As it was not possible to achieve a perfectly known distribution of spe- and dpe events, an also correlated tpe peak was further added to the fitting function to describe the present multi pe peaks. Additionally, a second noise peak, which is assumed to be originating from photoelectrons that did not get amplified properly and therefore called dynode peak, was also added to the fitting function to improve the fit around the noise peak even more.

The gains of the PMTs were found to be in the range between $2 \times 10^6 N_{se}$ and $3 \times 10^6 N_{se}$ for the most part as expected from previous calibrations. Most of the determined gains are attached to a χ_{red}^2 of the interval from one to two. A following test on the correlation between the area of the spe- and dpe peak failed at first glance but on the other hand shows where problems in the procedure exist. First, the intended distribution for noise-, spe- and dpe events that were approximated was not sufficient. This also can be concluded from the very existence of a tpe peak, as a tpe peak would not be visible in the current distribution as it would only make 0.002% of the events (Poisson distribution), resulting in 20 expected tpe

events for 1M events taken in total, whereas some histograms show the amplitudes of almost up to 10^3 events (e.g. PMT6). Further investigations should try to adjust the HV of the PMTs until all see the same total number of spe- and dpe events to check if P_2/P_1 converges to a constant value.

In conclusion it can be stated that the chosen fitting functions describe the histograms for the most part but there are still unknown factors missing that show in the flawed description of the noise peak and the slight oscillation in the residuals. For future gain calibrations a method has to be found to precisely determine the reached distribution of spe- and dpe events dependent on the LEDs intensity. Therefore the Gaussian addends could be constrained even more by correlating their areas to the distribution. Further the high voltage on some PMTs needs to be lowered to cause as few multi pe peaks as possible.

Using the ^{137}Cs source, an energy calibration and the determination of the energy resolution could be performed. Although the S2 spectrum could not be used, the measured ^{137}Cs S1 showed two clear peaks, that were fitted with a Gaussian each to ascertain their means. The mean value in pe units was matched with the 662 keV peak of the ^{137}Cs gamma decay for both peaks. In order to identify the real 662 keV peak the events got further analyzed and a high frequency of double scatter events that did not get identified by *PAX* was found. A cut on most of the double scatter events lead to the conclusion that the S1 peak around 513 pe is the actual 662 keV peak. This leads to a light yield of 0.78 pe/keV. The unknown signal in the spectrum requires further investigation. For now, the calibration source was static during the whole measurement. Changing the position of the source at a certain height around the detector may lead to a more homogeneous distribution of events in the x-y-level of the detector. Further the position of the source should be changed like suggested in [9] to imitate the performed Monte Carlo simulation while determining the position of the source relative to the TPC precisely. This should improve the quality of the results that were to be investigated in the future. The reason for not seeing a ^{137}Cs peak in the S2 spectrum is most likely a not sufficient liquid level inside the detector. A precisely controlled liquid level should therefore be more emphasized for future measurements. Additionally, further calibrations of the *Muenster xenon TPC* could consider implementing corrections for light collection efficiency and electron lifetime, as it is very common at its larger counterparts at the LNGS.

A Appendix

The following figures show a histogram for each of the 14 PMTs except PMT5, since PMT5 had technical issues during the measuring process of this thesis. Each of the histograms was fitted with the number of gaussians that provide the smallest χ_{red}^2 . At the end of the appendix a table shows a summary of all fit parameters used for each fit. The color-scheme is consistent through all histograms: The fit is colored red, the black gaussian is the noise peak, the pink one is the spe peak, the cyan one is the dpe peak, the dark blue one is the tpe peak and the green one is the dynode peak. Most of the histograms show oscillations in the residuals, which is usually an indicator of a problem in the fitting function and requires further investigation.

A.1 Histograms of the PMTs

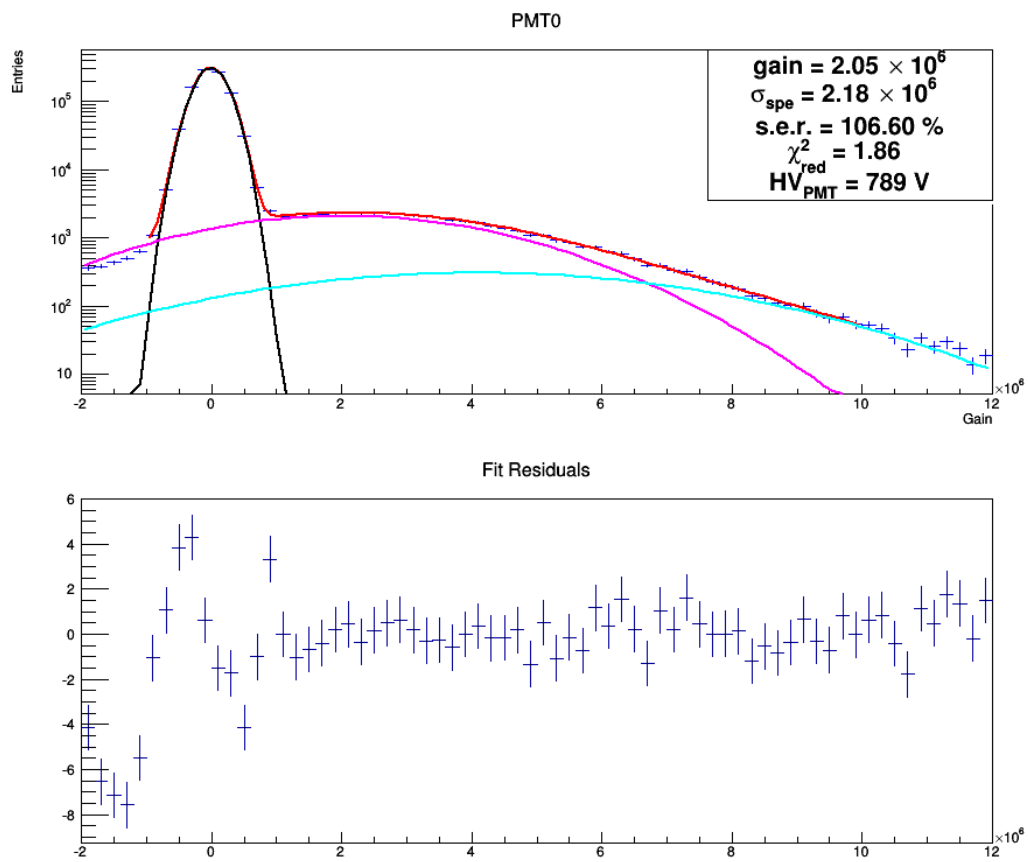


Figure A.1: Histogram of the data collected at PMT0.

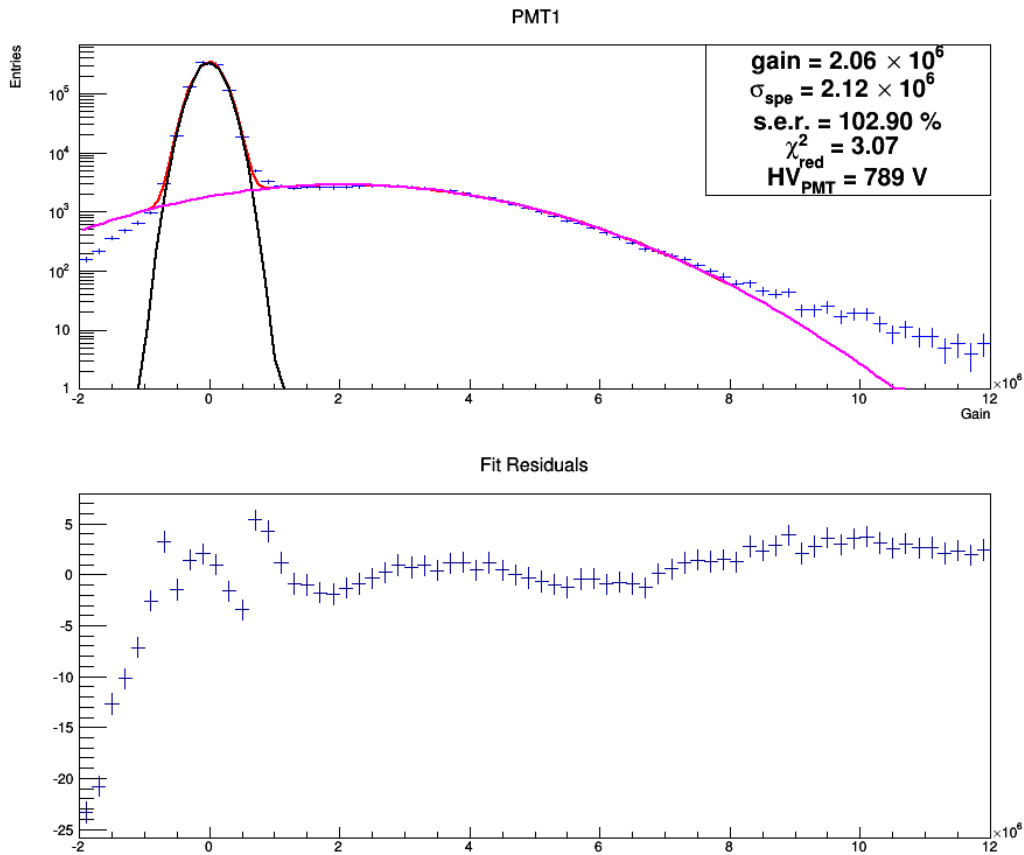


Figure A.2: Histogram of the data collected at PMT1 and fitted with $g_2(x)$. This fit can be considered flawed as is already stated by a worse χ_{red}^2 than at most of other fits. The residuals also show, that the fit lies above the actual data in the region of the spe peaks mean. The problem is, that a dpe peak is already constrained in his mean and width by the spe peak which results in the dpe peak not being able to describe the data past $8 \times 10^6 N_{se}$ without increasing the overall χ_{red}^2 . Also the residuals do not give a clear sign of how the fit would be possible to fix.

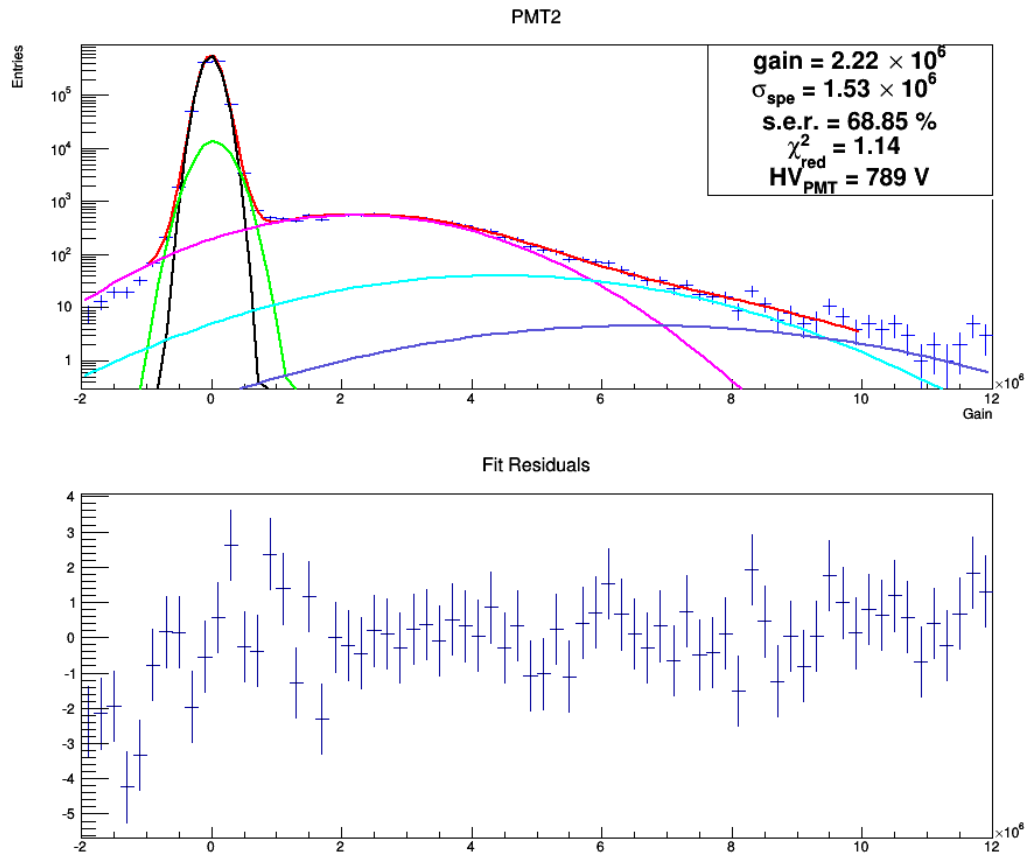


Figure A.3: Histogram of the data collected at PMT2.

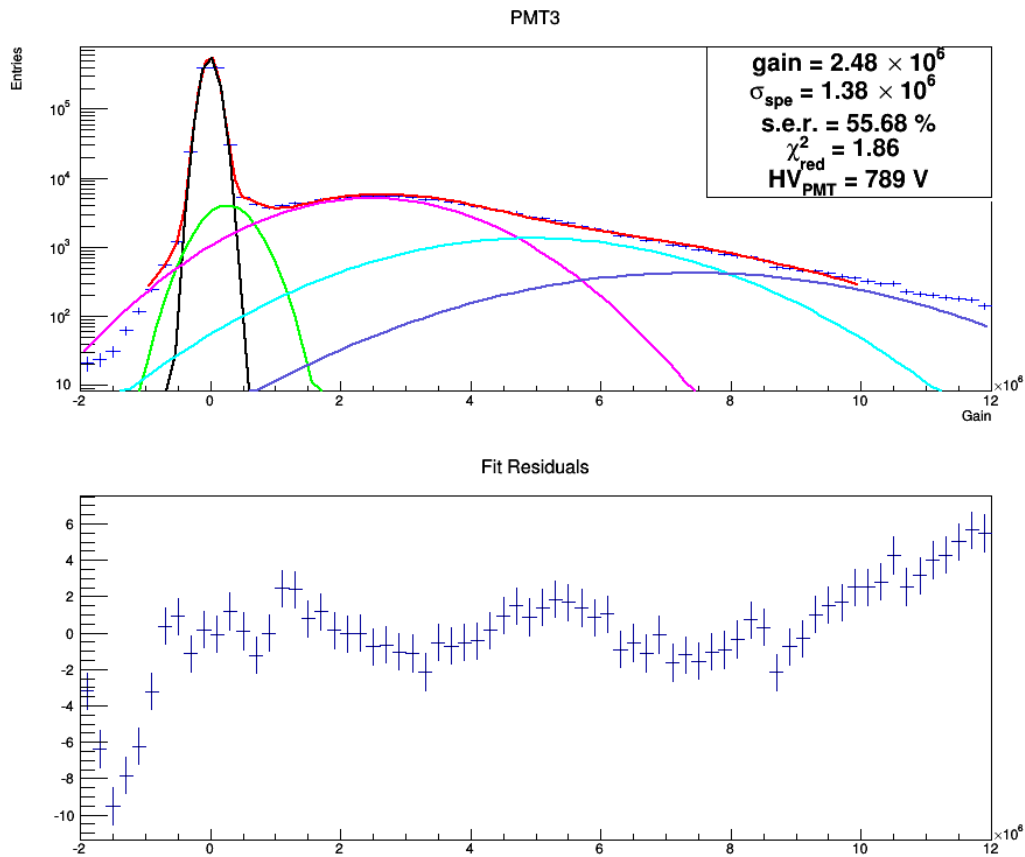


Figure A.4: Histogram of the data collected at PMT3. The histogram shows high count rates even at more than $10 \times 10^6 N_{se}$ which indicates a too high HV applied to the PMT. Also PMT3 is the center PMT of the bottom array so it is expected to see the most light of all PMTs. Problematic in this fit is the very large tpe peak in comparison to the dpe peak. In this case it could even be considered to add a gaussian for a correlated quadruple pe peak to the fitting function.

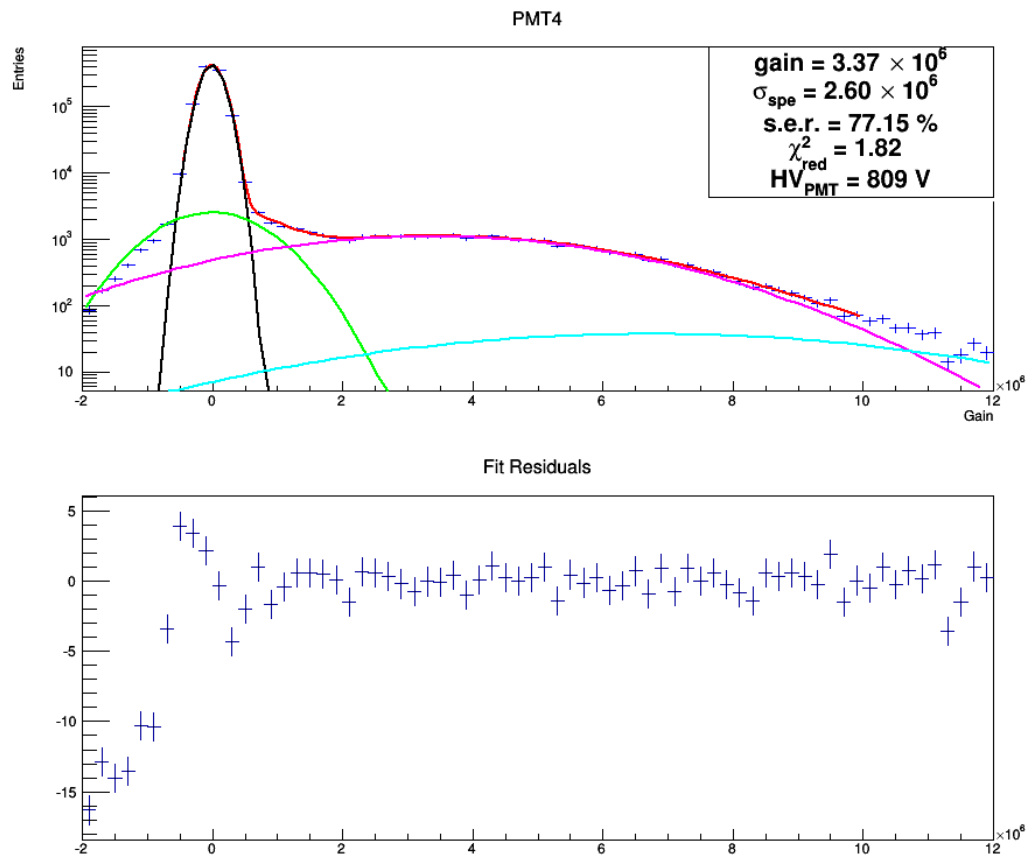


Figure A.5: Histogram of the data collected at PMT4.

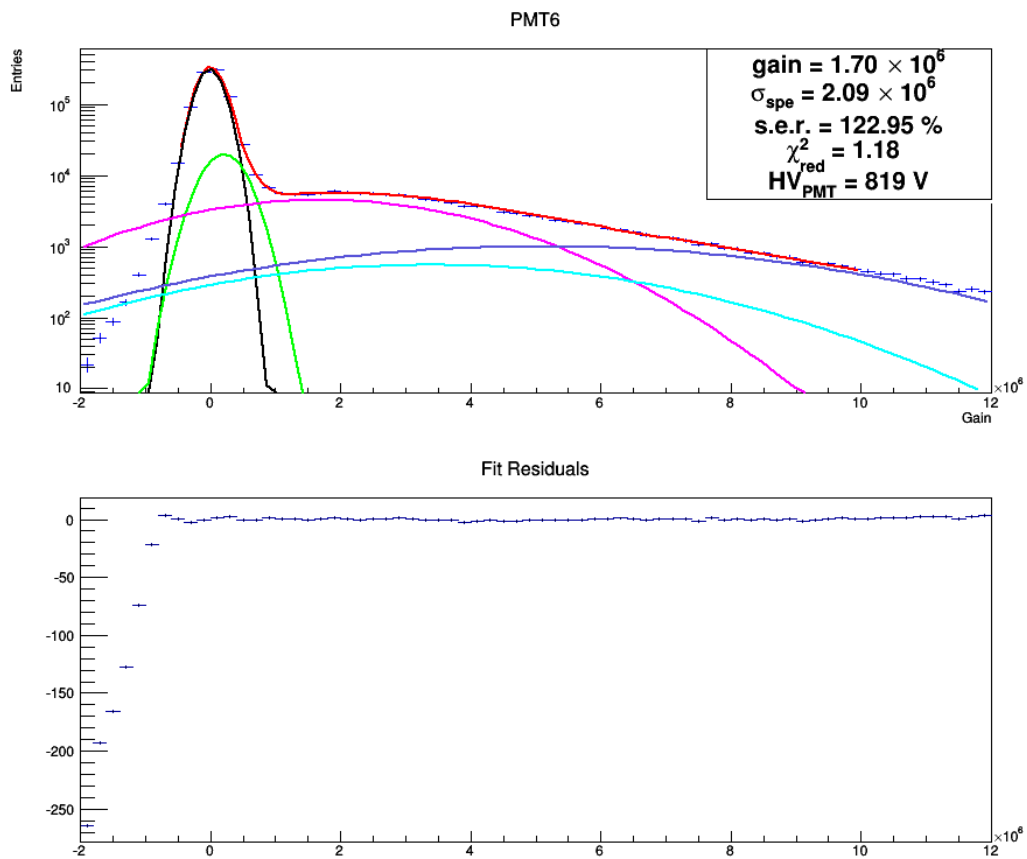


Figure A.6: Histogram of the data collected at PMT6. This histogram shows similar difficulties as the one of PMT3. Here the HV of the PMT6 can be considered to be too high. A quadruple pe peak could be added to lower the amplitude of the tpe peak

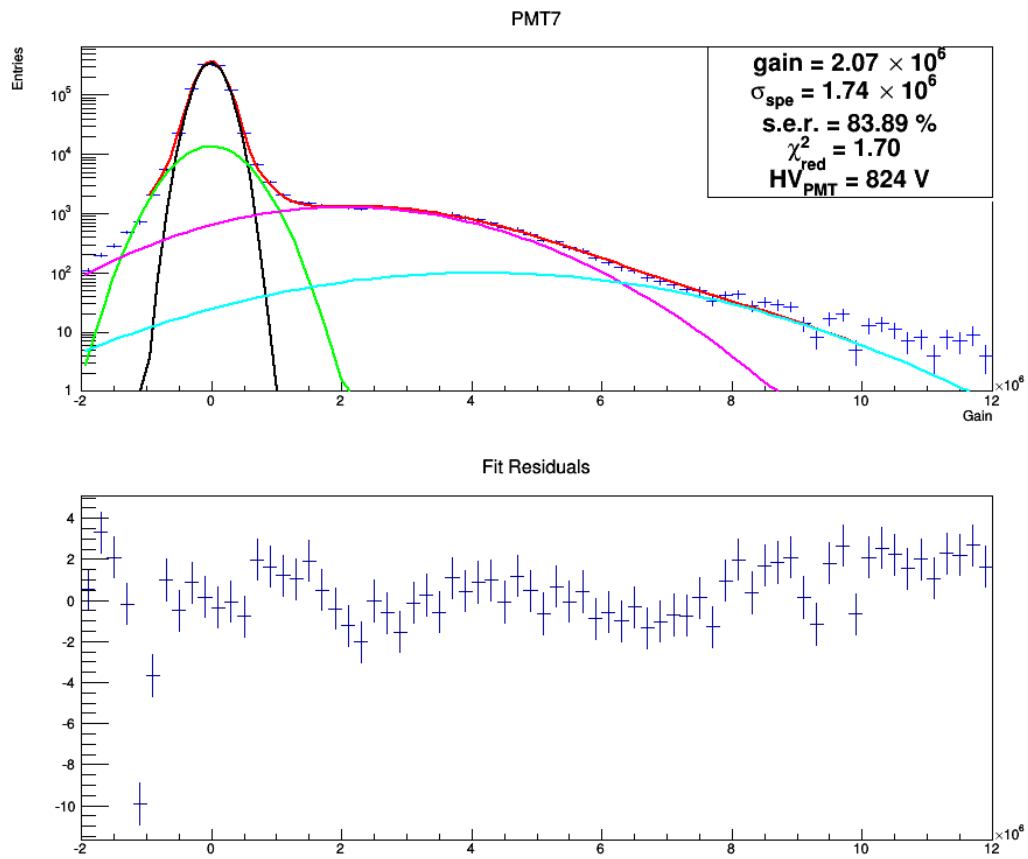


Figure A.7: Histogram of the data collected at PMT7. Here a tpe peak might seem needed but did not result in an overall improved fit.

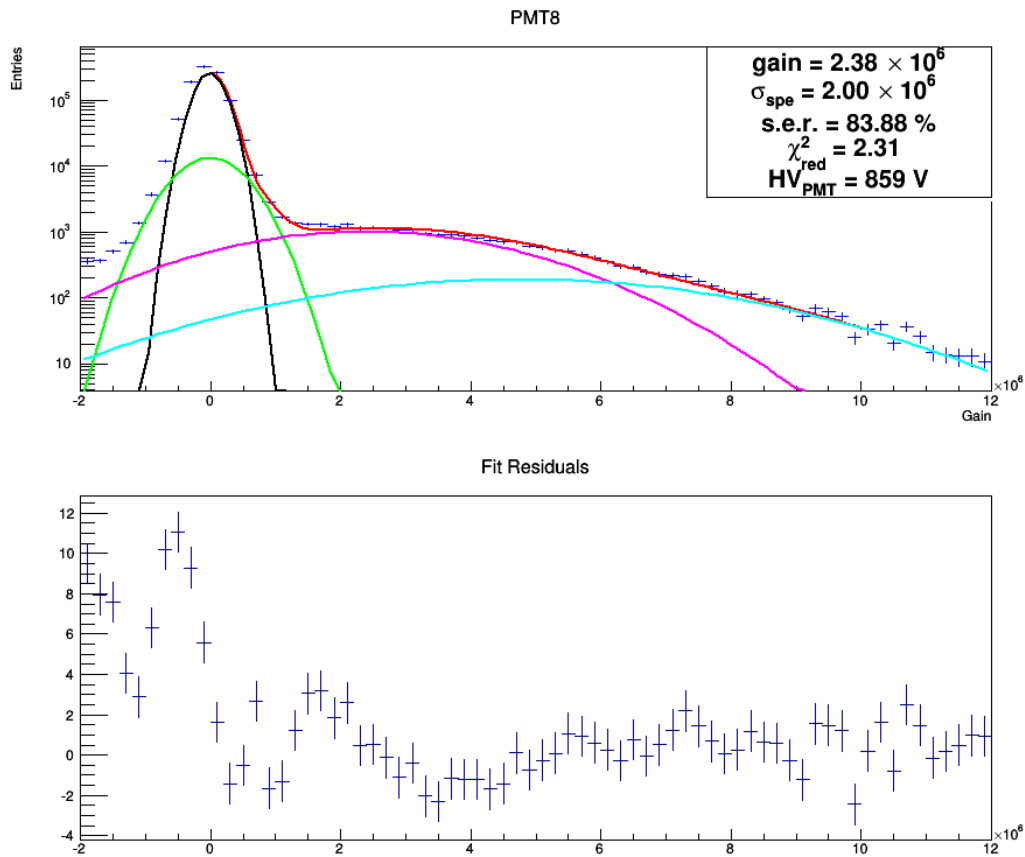


Figure A.8: Histogram of the data collected at PMT8. The residuals show problems with the fitting function that are not immediately obvious. The fitting function is not able to describe the whole problem. Further the fit parameter of the dpe amplitude got to the chosen upper limit, since otherwise the spe mean would immediately go towards zero and increase the χ_{red}^2 severely. So this fit has to be looked at carefully.

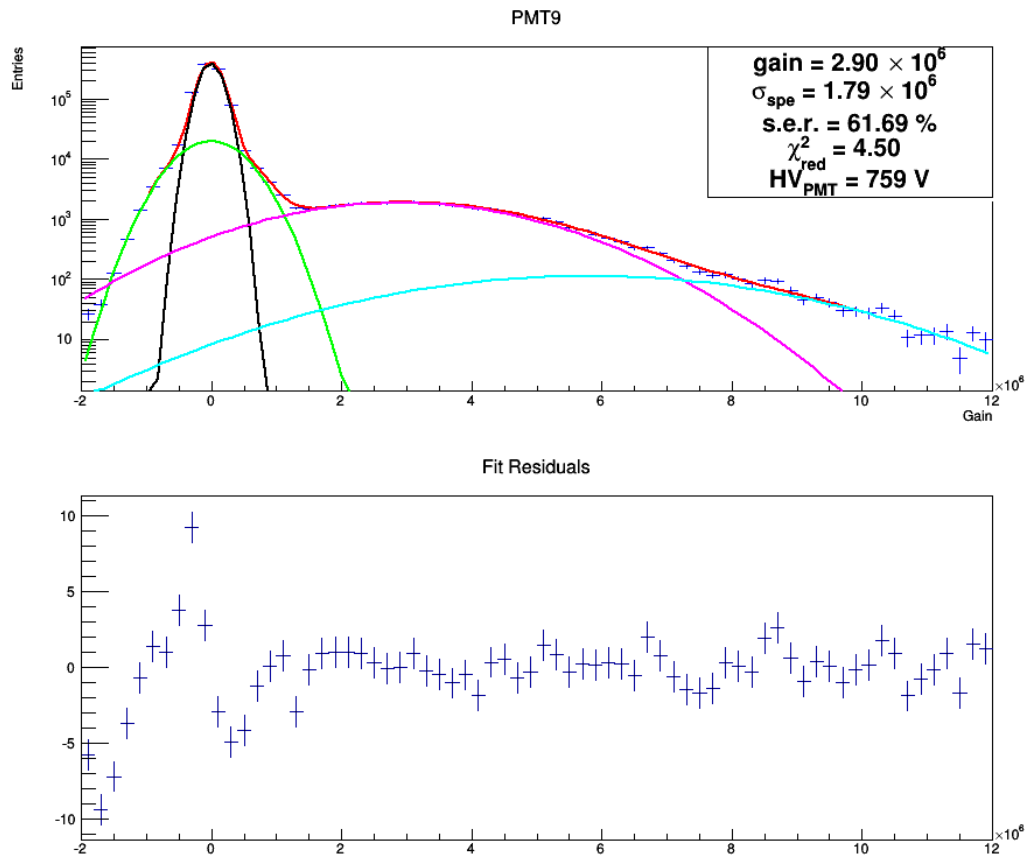


Figure A.9: Histogram of the data collected at PMT9.

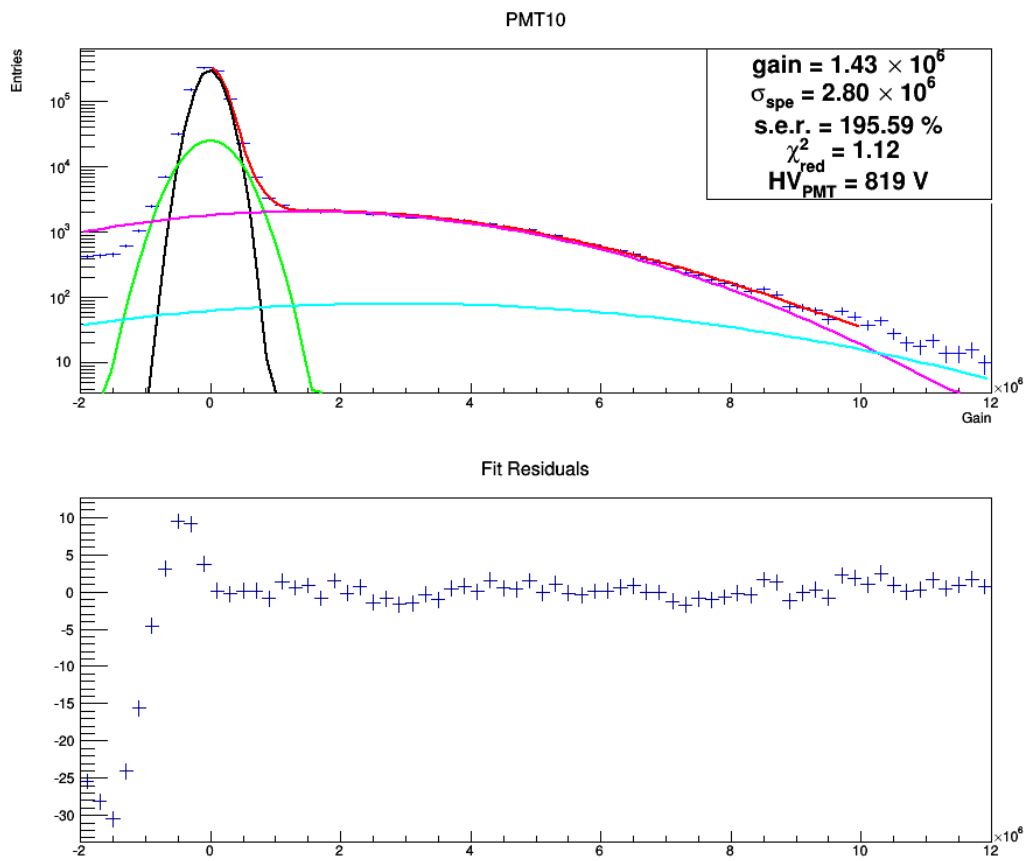


Figure A.10: Histogram of the data collected at PMT10.

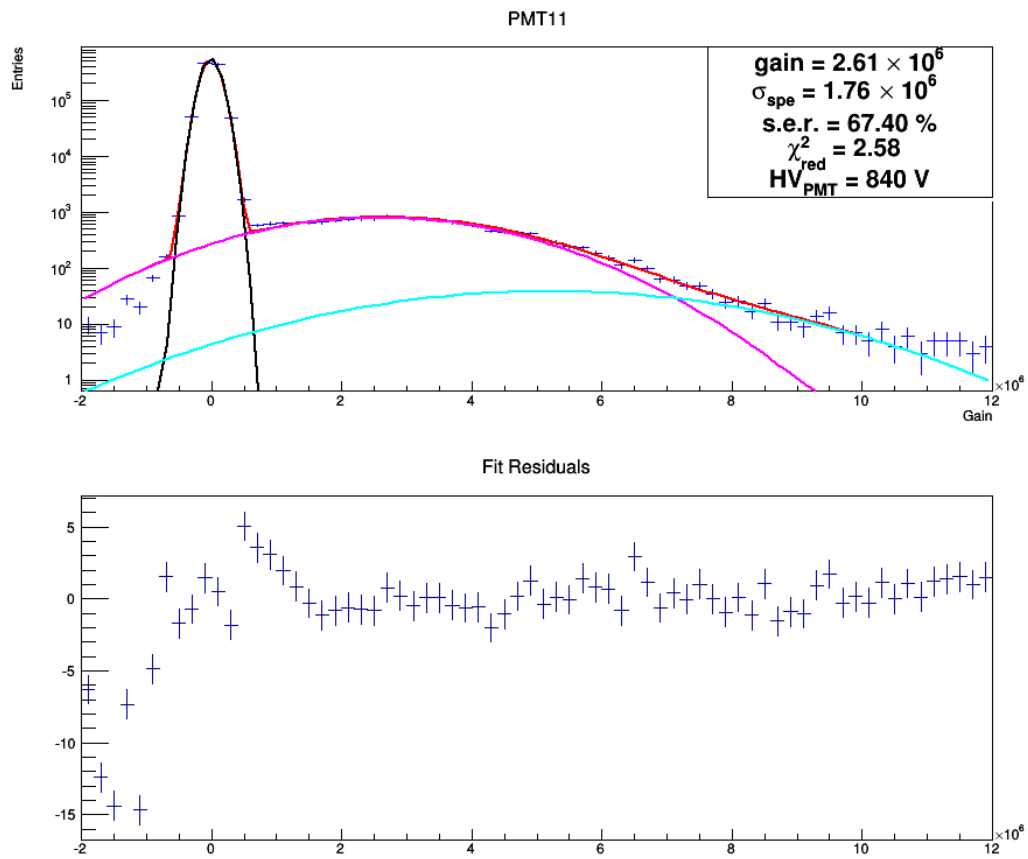


Figure A.11: Histogram of the data collected at PMT11. In this case the fit is not able to describe the valley between noise peak and spe peak. This might imply, that the spe mean got fitted at a too high value. A dynode peak also could not solve the problem.

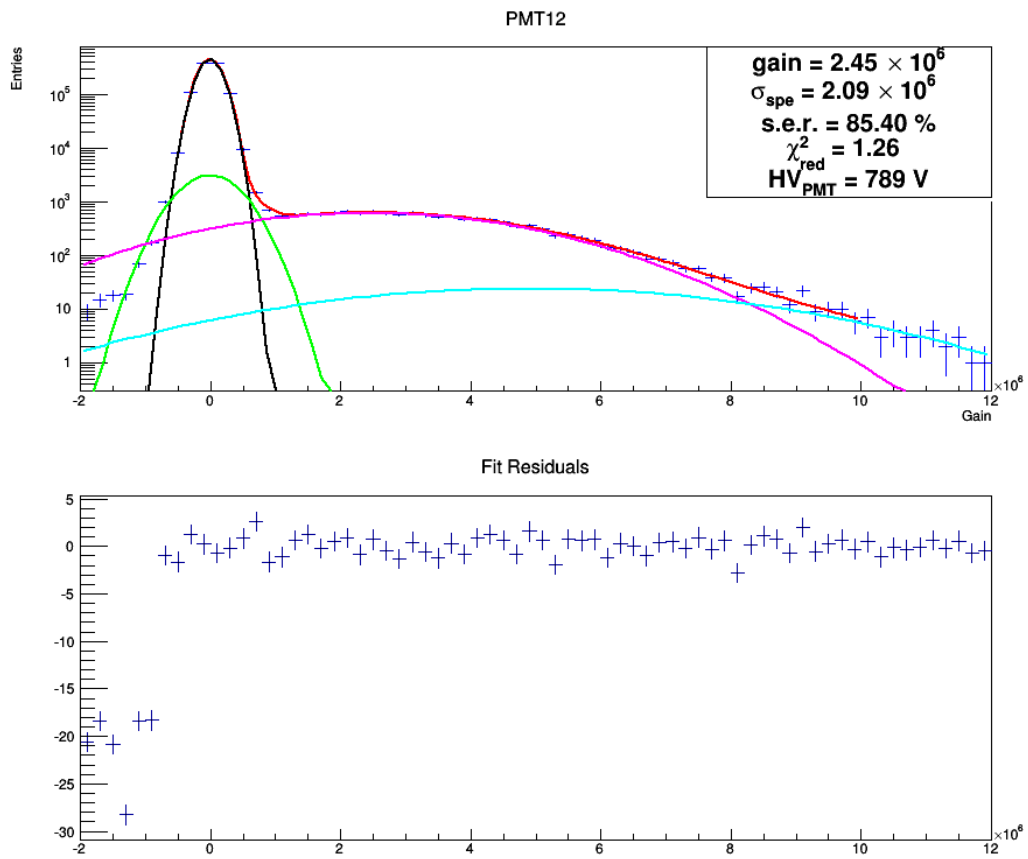


Figure A.12: Histogram of the data collected at PMT12.

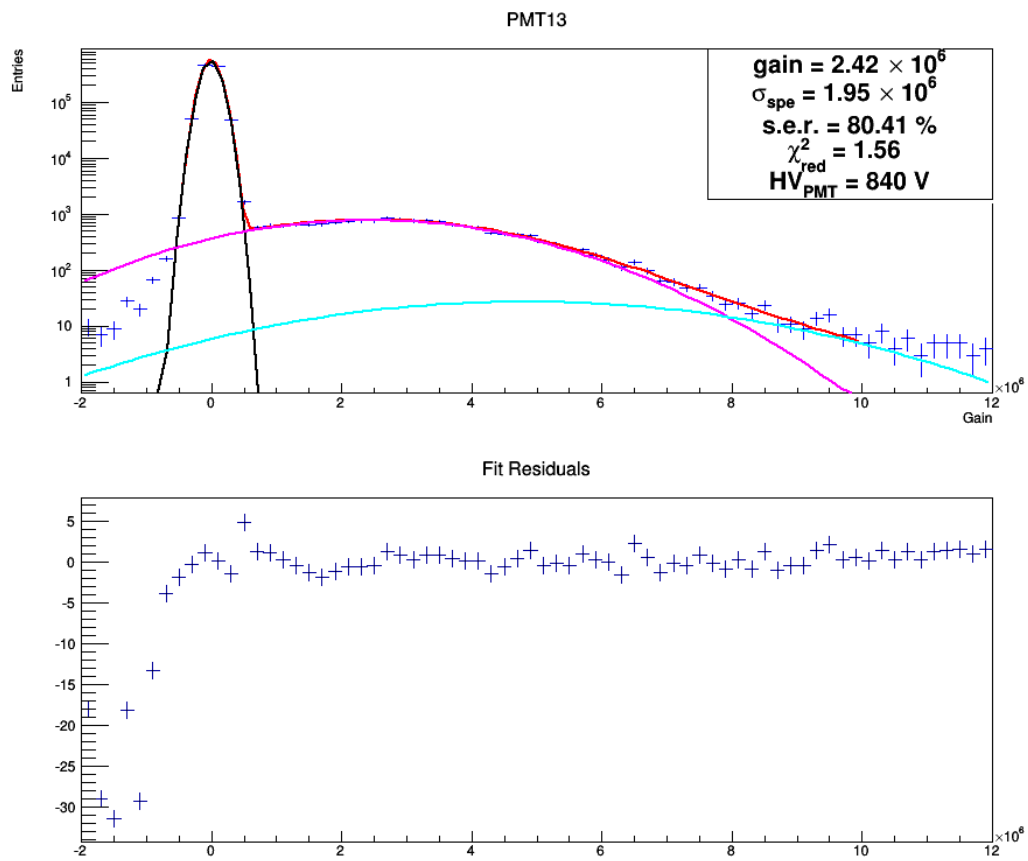


Figure A.13: Histogram of the data collected at PMT13.

A.2 Parameters used for the fits

A summary of the parameters used for each fit and the fit results. If a parameter is marked with “-”, the corresponding gaussian was not included in the fitting function.

Table A.1: Results for the fit parameters of all histograms

PMT	$A_n \times 10^5$	x_n	$\sigma_n \times 10^5$	$A_{dyn} \times 10^4$	$x_{dyn} \times 10^4$	$\sigma_{dyn} \times 10^5$
0	3.12±0.05	0	2.36±0.01	-	-	-
1	3.34±0.11	0	2.10±0.02	-	-	-
2	5.47±0.21	0	1.37±0.02	1.34±0.34	4.93±0.77	2.93±0.10
3	5.67±0.02	0	1.19±0.01	0.40±0.04	26.41±2.18	3.81±0.22
4	4.25±0.15	0	1.69±0.02	0.25±0.02	0 (fixed)	7.56±0.52
5	-	0	-	-	-	-
6	3.09±0.09	0	1.92±0.03	1.95±0.63	21.03±6.13	3.01±0.11
7	3.58±0.10	0	1.98±0.03	1.35±0.19	0 (fixed)	4.68±0.21
8	2.50±0.00	0	2.15±0.05	1.30±0.35	0 (fixed)	4.78±0.32
9	3.66±1.25	0	1.59±0.02	1.94±0.11	0 (fixed)	4.66±0.09
10	3.01±0.10	0	1.93±0.03	2.52±0.37	0 (fixed)	3.74±0.15
11	5.44±0.02	0	1.38±0.01	-	-	-
12	4.44±0.11	0	1.74±0.01	3.00±0.09	0 (fixed)	4.11±0.11
13	5.57±0.19	0	1.37±0.01	-	-	-

Table A.2: Continuation of the fit parameters of all histograms

PMT	$A_{spe} \times 10^3$	$x_{spe} \times 10^6$	$\sigma_{spe} \times 10^6$	$A_{dpe} \times 10^2$	$A_{tpe} \times 10$	χ_{red}^2	NDF
0	2.09±0.03	2.05±0.04	2.18±0.05	3.07±0.38	-	1.86	49
1	2.85±0.04	2.06±0.04	2.12±0.02	-	-	3.07	40
2	0.54±0.01	2.22±0.04	1.53±0.04	0.40±0.09	0.45±0.19	1.14	45
3	5.06±0.08	2.48±0.04	1.38±0.02	13.35±0.53	41.90±3.21	1.86	45
4	1.10±0.02	3.37±0.12	2.60±0.13	0.37±0.22	-	1.82	45
5	-	-	-	-	-	-	-
6	4.47±0.11	1.70±0.09	2.09±0.12	5.49±1.11	99.99±1.45	1.18	43
7	1.27±0.02	2.07±0.09	1.74±0.05	0.99±0.22	-	1.70	47
8	1.00±0.02	2.38±0.03	2.00±0.01 (limit)	1.90±0.00 (limit)	-	2.31	42
9	1.85±0.02	2.88±3.65	1.83±0.03	1.00±0.04	-	1.21	42
10	2.04±0.04	1.43±0.12	2.80±0.06	0.80±0.16	-	1.12	42
11	0.79±0.01	2.61±0.03	1.76±0.02	0.38±0.05	-	2.58	49
12	0.60±0.01	2.45±0.08	2.09±0.06	0.26±0.06	-	1.28	45
13	0.77±0.01	2.42±0.05	1.95±0.04	0.27±0.05	-	1.56	47

A.3 Example of a S1-S2 event

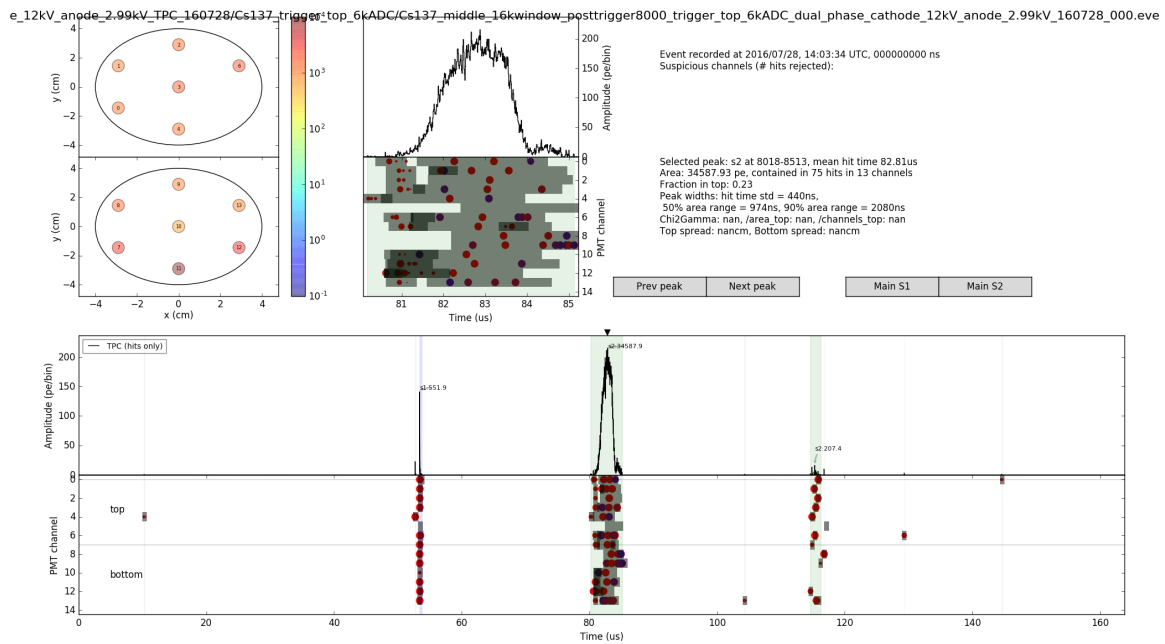


Figure A.14: Output of *PAX* for a perfectly matched S1 and S2. The small peak on the left of the waveform is the S1 and the large peak in the middle the S2 caused by the S1. The small peak on the right got wrongly identified as a S2 by *PAX*. On the top there are more useful information about the event, like for example how much intensity each PMT detected.

Bibliography

- [1] Planck Collaboration. Planck 2013 results. XVI. Cosmological parameters. 571:A16, November 2014. 1
- [2] The XENON collaboration, E. Aprile et al. The XENON100 dark matter experiment. *Astroparticle Physics*, 35:573–590, April 2012. 1, 9, 33
- [3] The XENON collaboration, E. Aprile et al. Physics reach of the XENON1T dark matter experiment. *Journal of Cosmology and Astroparticle Physics, Issue 4*, 4:027, April 2016. 1
- [4] Johannes Schulz. Design of a 2-phase xenon time projection chamber for electron drift length measurements, 2011. 2, 14
- [5] E. Aprile and T. Doke. Liquid xenon detectors for particle physics and astrophysics. *Reviews of Modern Physics*, 82:2053–2097, July 2010. 4, 6
- [6] National Institute for Standards and Technology. homepage: <http://physics.nist.gov>. 5, 7
- [7] T. Takahashi, S. Konno, T. Hamada, M. Miyajima, S. Kubota, A. Nakamoto, A. Hitachi, E. Shibamura, and T. Doke. Average energy expended per ion pair in liquid xenon. *Phys. Rev. A*, 12:1771–1775, Nov 1975. 6
- [8] National Nuclear Data Center. homepage: <https://www.nndc.bnl.gov>. 6, 7
- [9] Lutz Althüser. Geant4 simulations of the muenster dual phase xenon tpc, 2015. 7, 27, 29, 33, 36
- [10] G. Knoll. *Radiation Detection and Measurement*, volume 3. John Wiley & Sons, 2000. 8
- [11] Dr. Cecilia Levy Brown. *Light Propagation and Reflection off Teflon in Liquid Xenon Detectors for the XENON100 and XENON1T Dark Matter Experiment*. PhD thesis, WWU Münster, 2014.
- [12] Axel Buß. Characterisation of the muenster dual phase xenon tpc and of a newly developed magnetically piston pump. Master’s thesis, WWU Münster, 2016. 9

- [13] Hamamatsu Photonics K. K. *Photomultiplier Tubes: Basics and Applications*, 3a edition, 2007. 12